TÜRKİYE CUMHURİYETİ
ADANA ALPARSLAN TÜRKEŞ SCIENCE AND TECHNOLOGY UNIVERSITY

GRADUATE SCHOOL
MECHANICAL ENGINEERING DEPARTMENT

CONTROL OF THE FLOW DOWNSTREAM OF A BACKWARD-FACING STEP

AHMET REMZİ ERKOÇ

M.Sc.

ADANA 2024

TÜRKİYE CUMHURİYETİ
ADANA ALPARSLAN TÜRKEŞ SCIENCE AND TECHNOLOGY UNIVERSITY

GRADUATE SCHOOL
MECHANICAL ENGINEERING DEPARTMENT

CONTROL OF THE FLOW DOWNSTREAM OF A BACKWARD-FACING STEP

AHMET REMZİ ERKOÇ

M.Sc.

THESIS ADVISOR
ASST. PROF. DR. TURAL TUNAY

ADANA, 2024

ÖZET

GERİYE DÖNÜK BİR ADIMDA AŞAĞI AKIŞIN KONTROLÜ

Ahmet Remzi ERKOÇ
Yüksek Lisans, Makine Mühendisliği Anabilim Dalı
Danışman: Dr. Öğr. Üyesi Tural TUNAY

Ağustos 2024, 75 sayfa

Aktif ve pasif akış yöntemlerini kullanarak geriye dönük adım etrafındaki akışı kontrol etmek için nümerik bir çalışma gerçekleştirilmiştir. Coanda aktüatör aktif akış kontrol metodu olarak kullanılırken, eğimli çift basamaklı geriye dönük adım da pasif akış kontrol yöntemi olarak kullanılmıştır. Araştırma, basamak yüksekliği ve serbest akış hızı baz alınarak $Re_h = 6 \times 10^3$, 9.6×10^3 ve 20×10^3 Reynolds sayılarında gerçekleştirilmiştir. Geriye dönük adım üzerindeki akışın çözümü için, Spalart-Allmaras, gerçekleştirilebilir k-ε ve SST k-ω olmak üzere üç farklı türbülans modeli test edilmiştir. Deneysel verilerle karşılaştırıldığında, Spalart-Allmaras modeli yeniden bağlanma uzunluğu, X_r'yi, %0,95 hatayla tahmin ettiğini gösterdi. Ancak, SST k-ω modeli girdap bölgesinde eksenel hızı maksimum %5 hatayla tahmin etti. Akış kontrolü olmayan, değiştirilmemiş geriye dönük adım durumunda, yeniden bağlanma uzunluğu sırasıyla $Re_h = 6 \times 10^3$, 9.6×10^3 ve 20×10^3 için X_r/h = 4.40, 4.16, 4.20 şeklinde bulunmuştur. Coanda aktüatörü aracılığıyla yapılan aktif akış kontrolü sonucunda C_M = 0.02 momentum katsayısı kullanılarak, $Re_h = 6 \times 10^3$, 9.6×10^3, 20×10^3 için, yeniden bağlanma uzunluğu sırasıyla X_r/h = 1.0, 0.58 ve 0.56'ya düşmüştür. Daha büyük momentum katsayısı, yani $C_M \geq 0.06$ kullanıldığında girdap bölgesi tamamen ortadan kalktı. Eğimli çift basamaklı geriye dönük adım yoluyla pasif akış kontrolü durumunda, üst basamak yüzeyinin eğim açısı, $\alpha = 15^o$ ve alt basamak yüzeyinin, $\beta = 70^o$ kombinasyonları kullanılarak yeniden bağlanma uzunluğundaki maksimum bağıl yüzde azalma %20.2 olmuştur. Öte yandan, $\alpha = 75^o$ ve 90^o dahil olmak üzere diğer eğimli yüzey kombinasyonları, değiştirilmemiş BFS geometrisi ile elde edilenden daha uzun yeniden bağlanma uzunluğuyla sonuçlanmıştır.

Anahtar Kelimeler: Geriye dönük adım, Coanda Aktüatör, Eğimli adım, Yeniden bağlanma, Ayrılmış ve yeniden bağlanmış akış

ABSTRACT

CONTROL OF THE FLOW DOWNSTREAM OF A BACKWARD-FACING STEP

Ahmet Remzi ERKOÇ
M.Sc., Department of Mechanical Engineering
Supervisor: Asst. Prof. Dr. Tural TUNAY
August 2024, 75 pages

A numerical study was performed to control the characteristics of the flow through the backward-facing step with the aid of active and passive control methods. The Coanda actuator was used as the active flow control method while the inclined double backward-facing step surfaces were used as the passive flow control method. The investigations were performed for the Reynolds Numbers of $Re_h = 6 \times 10^3$, 9.6×10^3 and 20×10^3 based on step height, *h*, and the free stream velocity, U_∞. Three different turbulence models, i.e., Spalart-Almaras, realizable *k-ε* and SST *k-ω* turbulence models, were tested for the solution of the flow over the backward-facing step. The results, which were validated using the experimental data, shown that the Spalart-Allmaras model estimated the reattachment length, X_r, with an error of 0.95%. However, in the recirculation region, the SST *k-ω* estimated the axial velocity with a maximum error of 5%. In the case of an unmodified backward-facing step with no flow control, the reattachment length was found as X_r/h = 4.40, 4.16, 4.20 for $Re_h = 6 \times 10^3$, 9.6×10^3 and 20×10^3. As the results of the active flow control via the Coanda actuator, at the momentum coefficient of C_M = 0.02, the reattachment length was reduced to X_r/h = 1.0, 0.58, and 0.56 for $Re_h = 6 \times 10^3$, 9.6×10^3, 20×10^3, respectively. Using a larger momentum coefficient, i.e., $C_M \geq 0.06$, completely vanished the recirculation region. In the case of passive flow control via inclined double backward-facing step, the maximum relative percent reduction of the reattachment length was 20.2% using the combinations of the inclination angle of upper step surface, $\alpha = 15^\circ$, and lower step surface, $\beta = 70^\circ$. On the other hand, the other inclined surface combinations, including $\alpha = 75^\circ$ and 90°, resulted longer reattachment length than the one obtained with unmodified BFS geometry.

Keywords: Backward-facing step (BFS), Coanda Actuator, Inclined Step, Reattachment Length, Separated and reattached flow

TABLE OF CONTENTS

ÖZET i

ABSTRACT ii

TABLE OF CONTENTS iii

LIST OF FIGURES iv

LIST OF TABLES vi

LIST OF ABBREVIATIONS vii

LIST OF SYMBOLS viii

1. INTRODUCTION 1

2. THEORETICAL FOUNDATIONS AND LITERATURE REVİEW 2

3. MATERIAL AND METHODS 16

3.1. The Flow Geometry 16

3.2. The Governing Equation Of The Flow 17

3.2.1 Spalart Almaras Turbulence Model 18

3.2.2 SST k-ω Turbulence Model 20

3.2.3 Realizable k-ε Turbulence Model 22

3.3. The Boundary Conditions of the Computational Flow Domain 24

3.4. Details of the Computational Mesh and It is verification 25

4. RESULTS AND DISCUSSION 28

4.1. Assessment of the Results of Different Turbulence Models 28

4.2. Application of Different Flow Control Methods 35

4.2.1. The active flow control via the Coanda actuator 35

4.2.2. Inclined and double step 42

5. CONCLUSION 49

REFERENCES 50

APPENDIX

LIST OF FIGURES

Figure 1.1. Schematic view of the flow over a backward-facing step geometry……………...2

Figure 3.1. The geometrical details of the backward-facing step with Coanda actuator…......16

Figure 3.2. Boundary conditions of BFS geometry……………………………………...…24

Figure 3.3. Cp graph of three mesh for the a. Spalart Allmaras model, b. Realizable k-ε model c. SST k-ω model……………………………………………………………………..26

Figure 3.4. a. Mesh with coarse boundary layer b. Mesh with fine boundary layer……......27

Figure 4.1. Time-averaged streamlines, $\overline{\psi}$, and velocity magnitude $\overline{U} = \sqrt{\overline{u}^2 + \overline{v}^2}$, contours obtained by using different turbulence models……………………………………………29

Figure 4.2. Profiles of the time-averaged streamwise velocity component normalized with the free stream velocity, $\overline{u}/U_\infty$…………………………………………………………..…30

Figure 4.3. Time-averaged vorticity, $\overline{\omega}$, contours obtained by using different turbulence models……………………………………………………………………………………...32

Figure 4.4. Time averaged skin friction coefficient, $\overline{C_f}$, on the lower wall obtained by using different turbulence models. **………………………………………………………………**33

Figure 4.5. Time-averaged pressure coefficient, $\overline{C_p}$, on the lower wall of the channel obtained by using different turbulence models. ……………………………………….…………34

Figure 4.6. The reattachment length, X_r, with respect to the momentum coefficient, C_M , for different Reynolds numbers……………………………………………………………..35

Figure 4.7. Time-averaged streamlines, $\bar{\psi}$, and velocity magnitude, $\overline{U} = \sqrt{\bar{u}^2 + \bar{v}^2}$, contours obtained with and without Coanda blowing for $Re_h = 6x10^3$……………………………36

Figure 4.8. Time-averaged streamlines, $\bar{\psi}$, and velocity magnitude, $\overline{U} = \sqrt{\bar{u}^2 + \bar{v}^2}$, contours obtained with and without Coanda blowing for $Re_h = 9.6x10^3$……………………………38

Figure 4.9. Time-averaged streamlines, $\bar{\psi}$, and velocity magnitude, $\overline{U} = \sqrt{\bar{u}^2 + \bar{v}^2}$, contours obtained with and without Coanda blowing for $Re_h = 20x10^3$……………….……………39

Figure 4.10. Time-averaged vorticity magnitude, $\overline{\omega}$, contours obtained with and without Coanda blowing for $Re_h = 6x10^3$...40

Figure 4.11. Time-averaged vorticity magnitude, $\overline{\omega}$, contours obtained with and without Coanda blowing for $Re_h = 9.6x10^3$..41

Figure 4.12. Time-averaged vorticity magnitude, $\overline{\omega}$, contours obtained with and without Coanda blowing for $Re_h = 20x10^3$...41

Figure 4.13. The time-averaged streamlines, $\bar{\psi}$, and velocity magnitude, $\overline{U} = \sqrt{\bar{u}^2 + \bar{v}^2}$, contours obtained for different inclined step surface angle combinations, α=15° and β=45°, 60°, 75°……………………………………………………………………………………43

Figure 4.14. The time-averaged streamlines, $\bar{\psi}$, and velocity magnitude, $\overline{U} = \sqrt{\bar{u}^2 + \bar{v}^2}$, contours obtained for the combinations of inclined step surface angles of α=90° and β=15°, 30°, 45°……………………………………………………………………………………44

Figure 4.15. Time-averaged streamlines, $\bar{\psi}$, and velocity magnitude, $\overline{U} = \sqrt{\bar{u}^2 + \bar{v}^2}$, contours obtained for the combinations of inclined step surface angles of α=75° and β=15°, 30°, 45°……………………………………………………………………………………45

Figure 4.16. The time-averaged vorticity, $\overline{\omega}$, contours obtained for the combinations of inclined step surface angles of α=15° and β=45°, 60°, 75°…………………………………..46

Figure 4.17. The time-averaged vorticity, $\bar{\omega}$, contours obtained for the combinations of inclined step surface angles of α=90° and β=15°, 30°, 45°…………………………………..47

Figure 4.18. The time-averaged vorticity, $\bar{\omega}$, contours obtained for the combinations of inclined step surface angles of α=75° and β=15°, 30°, 45°…………………………………..48

LIST OF TABLES

Table 2.1. The summary of the results obtained in the previous studies conducted on BFS flow……………………………………………………………………………………………….3
Table 3.1. The maximum amount of the dimensionless wall thickness, y^+, of the meshes that were used in the mesh independency study and their reattachment results.………………….27

Table 4.1. The results of the dimensionless reattachment length, X_r/h obtained for the double backward facing step with different step surface inclination angles.……………………...…42

LIST OF ABBREVIATIONS

BFS	: Backward Facing Step
CFD	: Computational fluid dynamics
DBFS	: Double Backward Facing Step
DES	: Detached Eddy Simulation
DNS	: Direct Numerical Simulation
LDV	: Laser Doppler Velocimetry
LES	: Large Eddy Simulation
MHFS	: Multiple High-Frequency Stimulation
PIV	: Particle İmage Velocimetry
RANS	: Reynolds-Averaged Navier–Stokes
SIMPLEC	: Semi-Implicit Method for Pressure Linked Equations-Consistent

LIST OF SYMBOLS

h	: Step height
Re	: Reynolds number
$\mathbf{Re_h}$	: Reynolds number based on step height
U_∞	: Free stream velocity
ER	: Expansion ratio
H_{out}	: Height of outlet
H_{in}	: Height of inlet
X_R	: Reattachment length
AR	: Aspect ratio
δ	: Boundary layer thickness
C_p	: Pressure coefficient
C_f	: Skin friction coefficient
C_M	: Momentum coefficient
r	: radius
f	: frequency
St	: Strouhal number
C_D	: Drag coefficient
s	: Coanda inlet height
u	: X-velocity
y	: Y-velocity
d	: Distance
U_j	: Jet velocity
γ	: Transport variable
L_{ent}	: Length of inlet lower wall
L_o	: Length of outlet lower wall
P	: Pressure
α	: Upper inclination angle
β	: Lower inclination angle

$\boldsymbol{\rho}$	: Density
$\dot{\boldsymbol{m}}$	: Mass flow rate
$\boldsymbol{A_s}$	: Coanda cross-sectional area
$\boldsymbol{A_h}$	: Step cross-sectional area
$\tilde{\boldsymbol{v}}$	: Turbulent kinematic viscosity
$\boldsymbol{v}$	: Molecular kinematic viscosity
$\boldsymbol{Y_v}$	: Destruction of turbulent viscosity
$\boldsymbol{G_v}$	: Production of turbulent viscosity
$\boldsymbol{\mu_t}$	: Turbulent viscosity
$\boldsymbol{f_{v1}}$	: Viscous damping function
$\overline{\Omega}_{ij}$	: Mean rate of rotation tensor
$\boldsymbol{\Gamma}$	: Effective of diffusivity
$\boldsymbol{S'}$	: Scalar indication of the deformation tensor

1. INTRODUCTION

Flow separation is one of the most common phenomena in many industrial applications involving fluid flows, such as flow inside a combustor, flow behind a vehicle, or flow around a building (Wang et al., 2019). Flow separations generally cause unfavorable effects in fluid flows, such as pressure losses in a pipe flow or increased drag forces on a body immersed in a fluid and noise generations. Control of flow separations, therefore, has been one of the main challenges for the fluid dynamics society in the past decades.

The flow over a backward-facing step (BFS) possesses the general characteristics of separated and attached flows (Lee and Mateescu, 1998). Flow through the BFS contains a free shear flow separation, a vortex evolution, and a reattachment, essential features of a separated flow (Chen et al., 2018). Overall, the BFS geometry serves as a fundamental test case for studying complex flow phenomena, validating numerical methods, and advancing our understanding of fluid dynamics across a wide range of applications. Thus, the conclusions drawn from a study on the flow over a BFS provide useful information on more complex industrial flows, such as the wake flow of ground vehicles.

Additionally, the number of the study in the previous literature that investigates the application of the Coanda actuator and double backward-facing step to control the flow over the BFS is limited. Thus, the present study aims to improve the knowledge on the abovementioned subjects.

The present study aimed to search for an effective flow control method to control the characteristics of a separated flow downstream of a backward-facing step, BFS, e.g., smaller reattachment length, X_r. Thus, for that purpose, the performance of an active flow control method, e.g., a Coanda actuator, and a passive flow control method, e.g., double inclined backward-facing step, was employed to the flow through a BFS. Investigations were performed using numerical methods with the aid of a commercial CFD solver, ANSYS Fluent. The rest of the article consists of Theoretical foundations and literature review, material and methods, results and discussion, and conclusion.

2. THEORETICAL FOUNDATIONS AND LITERATURE REVIEW

The flow field downstream of a BFS is generally divided into four regions, e.g., a separated shear layer region, a recirculation region under the shear layer, a reattachment region, and an attached/recovery region (Chen et al., 2018). A schematic view of the flow over a backward-facing step is shown below.

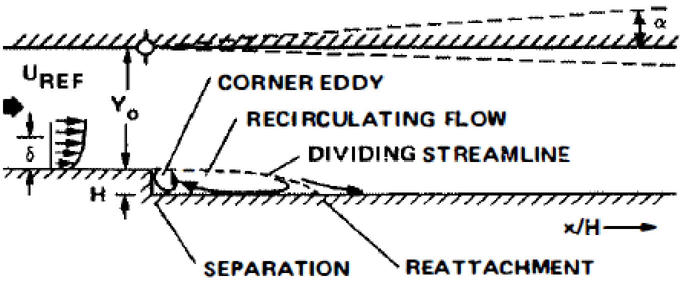

Figure 2.1. Schematic view of the flow over a backward-facing step geometry (Wilcox,2006).

The previous studies revealed that the length of the separated flow region downstream of a BFS depends on Reynolds number, Re, step height, *h*, and boundary layer thickness, δ, of the oncoming flow (Eaton and Johnston, 1981). Furthermore, Uruba et al. (2007) specified that the reattachment of the flow downstream of a BFS is a highly non-stationary dynamical process so the zone reattachment needs to be discussed rather than the point and the line reattachment when describing it. Additionally, the pressure coefficient, C_p, and skin friction coefficient, C_f, show a drop near the step of a BFS and then gradually increase in the downstream flow (Chen et al., 2018). There is a low-static pressure region under the shear layer and a part of the reattached flow recirculates back upstream forming a recirculating flow region due to low static pressure region (Li et al., 2020). Additionally, the wall shear stress takes negative values in the large part of the recirculation region downstream of the BFS (Tihon et al., 2001; Al-Jelawy et al., 2016; Chen et al., 2018). Tihon et al. (2001) showed that the skin friction coefficient is decreased by increasing the Reynolds Number.

Armaly et al. (1983) studied the relation between the Reynolds number and the reattachment length in the Reynolds number range of $70 < Re_h < 8000$ based on the step height, h, and the velocity of the free stream flow, U_∞. Their results showed that the reattachment length increases with an increase in Reynolds number in the laminar flow regime. However, the reattachment length decreases and reaches the minimum value at approximately $Re_h = 5500$ in transitional and turbulent flow regimes. Then, the reattachment length increases a little with Reynolds number at $Re_h > 6600$. Similarly, Chun and Sung (1996) showed that the reattachment length increased when Reynolds number increased by using different Reynolds number in the solution of the flow through a BFS, e.g., they found $X_r/h = 6.85$ at $Re_h = 13 \times 10^3$ while $X_r/h = 7.8$ at $Re_h = 33 \times 10^3$. Additionally, Durst and Tropea (1983) showed that the reattachment length increased with expansion ratio, H_o/H_i. Similar results can be concluded when considering the studies of Avancha and Pletcher (2002) and Barri and Andersson (2010) conducted at close Reynolds numbers in which the expansion ratio in their studies was $H_o/H_i = 1.5$ and 2, respectively, i.e., the reattachment length was $X_r/h = 6.1$ in the study of Avancha and Pletcher (2002) while it was $X_r/h = 7.1$ in the study of Barri and Andersson (2010). The summary of the results obtained in the previous studies conducted on the investigation of the flow over a BFS is presented in Table 1. In the table, H_o/H_i denotes the expansion ratio of the channel, Re_h denotes the Reynolds number, X_r/h denotes the dimensionless reattachment length and δ/h denotes the dimensionless boundary layer thickness.

Table 2.1. The summary of the results obtained in the previous studies conducted on BFS flow.

Study	H_o/H_{in}	Re_h	Method	X_r/h	δ/h	Flow Control
Wu et al. (2013)	1.01	3.4×10^3	PIV	4.25	8	Rough surfaces
Kostas et al. (2002)	1.02	4.6×10^3	PIV	4.8	5.25	-
Ma et al. (2017)	1.02	20×10^3	PIV	7.1	0.5	-
Ma et al. (2016)	1.04	20×10^3	PIV	7.1	0.5	Vortex generators
Chovet et al. (2018)	1.04	30.4×10^3	PIV	5.29	-	Forced flow
Nakagawa and Nesu (2010)	1.07	6×10^3	LDA	5.2	-	-
Li et al. (2020)	1.08	9.63×10^3	PIV	4.2	-	-

Sujar-Garrido et al. (2015)	1.1	30×10^3	LDV	5.85	-	DBD Plasma actuator
Benard et al. (2016)	1.1	30×10^3	PIV	5.9	-	DBD Plasma Actuator
Uruba et al. (2007)	1.1	35×10^3	Exp	6.1	0.12	Wall jet, Suction, Blowing
Addad et al. (2003)	1.1	170×10^3	LES	4	0.7	Acoustic source identificati on
Al-Jelawy et al. (2016)	1.125	57×10^3	k- ω SST Spalart Almaras	5.56 6.10	1.49	-
D'Adamo et al. (2014)	1.14	1.52×10^3	PIV	5.7	-	DBD Plasma actuator
Durst and Tropea (1983)	1.14 1.14 2.05 2.05	6×10^3 13×10^3 3×10^3 11×10^3	Exp	5.3 5.8 9 8.6	-	-
Khuwaranyu and Putivisutisak (2009)	1.2	5×10^3	k-ω – LSC	6.28	-	-
Bredberg and Davidson (2004)	1.2	5.1×10^3	k-ω (standard)	6.28	-	-
Kang et al. (2002)	1.2	5.1×10^3	LES	6.2	1.34	-
Le et al. (1997)	1.2	5.1×10^3	DNS	6.28	-	-
Kapiris and Mathioulakis (2014)	1.22	6.94×10^3	PIV	4.27	-	-
Okada et al. (2012)	1.25	5×10^3	LES	5.85	-	Synthetic jet
Huang and Fiedler (1997)	1.25	4.3×10^3	DPIV	4.95	-	
Schram et al. (2004)	1.25	5.1×10^3	PIV	5.24		-
Tihon et al. (2001)	1.4	4.8×10^3	Electrodiffus ion technique	5.1	-	-
Spazzini et al. (2001)	1.45	3.5×10^3 5.1×10^3 10×10^3 16×10^3	DPIV	5.05 5.39 6.14 6.54	-	-
Yoshioka et al. (2001)	1.5	3.7×10^3	PIV	5.5	-	Periodic perturbation
Avancha and Pletcher (2002)	1.5	5.54×10^3	LES	6.1	-	Heat transfer
Dejoan and Leschziner (2004)	1.5	3.7×10^3	LES	7	-	Jet flow
Furuichi et al. (2004)	1.5	5×10^3	LDV	6	--	-
Bouda et al. (2008)	1.5	7.6×10^3	PIV	4.5	1	Wall jet

Rhee and Sung (1999)	1.5	33×10^3	k-ε- f	7.3		Oscillating jet
Chun and Sung (1996)	1.5	33×10^3 23×10^3 13×10^3	LDV	7.8 7.2 6.85	0.41 0.38 0.28	Oscillating jet
Mehrez et al. (2010)	1.5	33×10^3	LES	7.2	-	Periodic perturbation
Choi and Kim (2020)	1.5	47.6×10^3	k–ε (standard) RNG model NLEVM EARSM	5.88 6.2 6.85 7.36	-	-
Otügen (1991)	1.5	8.3×10^3	LDA	6.3	0.044	-
Kasagi and Matsunaga (1995)	1.504	5.54×10^3	PTV	6.51	-	-
Fessler and Eaton	1.66	18.4×10^3	LDA	7.4	-	-
Kumar et al. (2020)	1.94	7×10^3 7.5×10^3 8×10^3 8.5×10^3 9×10^3	Standard k-ε	5.91 5.94 5.97 5.98 6.01	-	-
Pont-Vilchez et al. (2019)	2		DNS	8.8		-
Lee and Mateescu (1998)	2	0.8×10^3	MHFS	6.45	-	-
Hossain et al. (2013)	2	0.1×10^3 0.5×10^3 1×10^3	Num	3.8 10.4 8.6	-	-
Barri and Andersson (2010)	2	5.6×10^3	DNS	7.1	-	-
Wang et al. (2019)	2	4.4×10^3 9×10^3	PIV	6.1 7	-	-
Louda et al. (2013)	2	15×10^3	EARSM PIV	8.53 8.2	-	Inclined step
Papadopolous and Otügen (1995)	2	26.5×10^3	LDA	8.2	0.16	-
Juste et al. (2016)	2	0.2×10^3 0.3×10^3 0.5×10^3 0.7×10^3	LES	4.9 6.2 9.8 13.5	-	-
Rani et al. (2007)	2.02	0.2×10^3 0.4×10^3 0.6×10^3 0.8×10^3	Num	4 7.2 10.8 12.8	-	-
Munters et al. (2022)	2.25	6.4×10^3	k- ω SST	11	-	-
Eiyad Abu-Nada (2008)	3	0.6×10^3	Num	2	-	-
Yu et al. (2024)	-	24×10^3	DNS	12.1	-	-
Present Work	1.08	6×10^3 9.6×10^3	Spalart Allmaras	4.4 4.16	- -	- -

	20×10^3		4.2	-	-
	6×10^3	Spalart Allmaras	1	-	Coanda
	9.6×10^3		0.5	-	Coanda
	20×10^3		0.7	-	Coanda

The shear layer forming downstream of a BFS possesses a vertically oscillating motion interacting with the recirculation region that varies in size and causes the reattachment point to move back and forth in the axial direction of the flow. The scale of the shear layer's oscillating motion is up to approximately one step height. Additionally, most of the turbulence within the shear layer is generated by this oscillating motion occurring in its latter half (Ma and Schröder, 2017; Ma et al., 2022 a,b). Accordingly, Kasagi and Matsunaga (1995) stated that the highest values of Reynolds stresses were detected right before the reattachment point, i.e., in the latter half. Furthermore, Ma et al. (2022 a,b) stated that the separated shear layer was two-dimensional in the first half of the reattachment length from the step edge in the axial direction whereas it developed three-dimensional structures in the latter half. They also showed the existence of the spanwise coherent structures which affected the convection velocities of the coherent structures in the second half of the shear layer. These spanwise coherent structures were described as large as two-step heights and had frequency patterns similar to the vertical oscillations of the shear layer.

Detailed analysis of the flow through a BFS revealed the unsteady and three-dimensional nature of the longitudinal and spanwise oscillating flow motions downstream of the BFS, e.g., formations of vortex stretching, roll-up of vortex lines, vortex tubes (Sheu and Rani, 2006; Rani et al., 2007). For example, Sheu and Rani (2006) indicated that the roll-up shear-layer hovering vortices starts the Kelvin–Helmholtz like instability which are observed near the step. The Kelvin–Helmholtz vortices evolved into lambda-shaped vortices that struck the step wall and stretched into hairpin-like vortices. Moreover, a stationary helical vortex flow is created by a pair of counter-rotating helical cells arranged in a double helix structure that encircles the vortex tube (Rani et al., 2007). Finally, Schäfer et al. (2009) reported the oscillations of the secondary recirculation bubble at the upper channel wall with an expansion ratio of $H_o/H_i = 2.02$ besides the oscillations of the primary recirculation region on the lower channel wall. The formation of this secondary recirculation bubble at the upper channel wall was attributed to the local pressure minima found in the shear-layer vortices.

Besides understanding the characteristics of the separated and attached flow as mentioned above, the BFS geometry is also useful in investigating the performance of turbulence models to capture the flow characteristics because it provides controlled but challenging flow features, e.g., the flow separates always at the top corner of the step forming unsteady wake and free shear layer (Wilcox, 2006). Researchers often use experimental data and computational simulations of flows over backward-facing steps to assess the accuracy and performance of turbulence closure models. Thus, in the previous literature, many studies employed the BFS geometry in assessing the performance of turbulence models (Driver and Seegmiller, 1985; Gatski et al., 1996; Ko, 1999; Bredberg et al., 2002; Munter et al., 2022).

Driver and Seegmiller (1985) investigated the performance of eddy-viscosity turbulence models, i.e., k-ε, and algebraic-stress turbulence models (ASM), by comparing them with their experimental data. They showed that the modified algebraic-stress model (ASM) improved the results of unmodified ASM and the unmodified k-ε model while it overpredicts the dissipation rate. Additionally, Gatski et al. (1996) stated that the standard k-ε model underestimated the position of the reattachment point by 11% compared to the predictions made by the nonlinear k-ε model. The use of an isotropic eddy viscosity assumption in standard k-ε model and its variants resulted inaccurate predictions for normal Reynolds stresses that cause inaccurate predictions of the reattachment length (Thangam and Speziale, 1992). Additionally, the standard k-ε model can produce unphysical results, e.g., negative values for turbulent kinetic energy, k, or turbulent dissipation rate, ε.

The realizable k-ε model was suggested by Shih et al. (1995) which was designed to better capture turbulence anisotropy by modifying the eddy viscosity formulation to provide more accurate predictions in flows where turbulence structures are not isotropic, such as near walls and in separated flows. The realizable k-ε model introduces enhancements in the formulation of the eddy viscosity and additional constraints to ensure that the model produces physically valid predictions of k and ε to improve physical realism and accuracy in predicting turbulent flows. Additionally, the realizable k-ε model is particularly beneficial for complex flows, such as those involving separations, reattachments, and recirculation zones as in flow over a BFS. Accordingly, Shih et al. (1995) reported that the realizable k-ε model solved the reattachment length with an error of less than 2% when compared with the corresponding experimental results of Driver and Seegmiller (1985) for the case of smaller step height.

Additionally, Wilcox (2006) stated that the Spalart-Allmaras model predicted the location of the reattachment point within 3% of the experimental data obtained by Driver and Seegmiller (1985). Bredberg et al. (2002) presented the importance of cross-diffusion terms in removing the freestream sensitivity with respect to ω for free shear flows by suggesting an improved k-ω turbulence model that needed neither wall-function nor wall-distance information. Finally, Munter et al. (2022) compared the results of different turbulence models, e.g., scale resolving, Reynolds-averaged and hybrid models, obtained for the flow over a BFS with a $Re_h = 6.4 \times 10^3$ and $H_o/H_i = 2.25$. Their results showed that DES and IDDES models which employ wall-modelled LES gave more accurate results whereas SAS and DDES were unsuccessful. They stated that the DDES suffered from Model-Stress Depletion, MSD, while SAS gave similar results with RANS.

Scale-resolving turbulence models, e.g., DNS and LES, allowing accurate stability analysis, were also employed in the previous studies for the solution of the flow through a BFS (Kaiktsis et al., 1991, 1996; Neto et al., 1993; Le et al., 1997). Thus, the characteristics of the average flow through a BFS which shows convective or absolute instability were revealed (Kaiktsis et al., 1991, 1996). These studies showed that, in the absence of any external disturbances, the final state of the flow over a BFS was independent of time for $Re < 2500$ while self-disturbances in the fluid flow grew as it moved over a BFS for $700 < Re < 2500$. On the other hand, any external excitations might end up with a time-dependent flow. For example, for small-amplitude monochromatic excitation, the flow exhibited time-periodic behavior when perturbed near the shear layer frequency, but it remained unchanged when the excitation frequency was high. On the other hand, when random noise was used as the input, the flow exhibited unsteady behavior with a fundamental frequency near the shear layer frequency. (Kaiktsis et al., 1996). Furthermore, calculations for $H_o/H_i = 5$ revealed that the eddy structure of the flow exhibited notable similarities to forced plane mixing layers, i.e., large billows formed behind the step with intense longitudinal vortices stretched between them. (Neto et al., 1993).

In addition to the abovementioned previous studies, the BFS geometry was the subject of many studies including heat transfer (Avancha and Pletcher, 2002; Yamada and Nakamura, 2016; Abu-Nada, 2008), two-phase flow (Barton, 1997; Benavides and van Wachem, 2009), biofluid (Hammand, 2015), acoustics (Addad et al., 2003). Backward-facing steps are utilized in heat transfer applications to enhance convective heat transfer. The recirculation zone formed downstream of the step can increase heat transfer rates by promoting mixing and increasing the contact area between the fluid and the solid surface. For example, Yamada and Nakamura (2016) revealed that the heat transfer rate increased due to the forward and downward flow in the near-wall region, with the viscous sub-layer playing a crucial role in regulating this rate. Additionally, Avancha and Pletcher (2002) employed LES to investigate flow through BFS including a uniform wall heat flux with different levels through the bottom wall downstream of the BFS at Re_h= 5540. They showed that the Stanton number profiles exhibited a remarkable similarity with the fluctuating skin-friction profiles. Moreover, Abu-Nada (2008) used different nanoparticles, e.g., Cu, Ag, TiO2, with different volume fractions in the fluid flow through a BFS to investigate heat transfer. It was found that, for Cu nanoparticles, the Nusselt number increased at the top and bottom walls, except in the primary and secondary recirculation zones where the enhancement was minimal. It was observed that outside the recirculation zones, nanoparticles with high thermal conductivity, like Ag or Cu, led to greater increases in the Nusselt number. Conversely, within the recirculation zones, nanoparticles with lower thermal conductivity, such as TiO2, provided better improvements in heat transfer. As for the use of BFS geometry to investigate flows including two-phase fluids, Barton (1997) studied the effects of buoyancy and thermophoresis on the laminar flow of fluid including particles suspended within it. He found that the size of the recirculation region increased when low-Stokes number particles were added to the flow. Benavides and van Wachem (2009) addressed the importance of turbulent characteristics for accurately predicting the mean motion of the dispersed phase and the modulation of turbulence in the continuous phase. Hammand (2015) investigated the characteristics of human blood flow through a BFS geometry to understand the effects of several factors, e.g., upstream flow conditions and geometrical features and rheology, on the flow characteristics of the blood flow. The results of the study revealed that the hemorheological properties of the blood are less effective than the upstream flow conditions, e.g., inflow velocity profile, on the characteristics of the separated flow downstream of the BFS.

Mushyam et al (2016) conducted a numerical study at low Reynolds numbers ranging from 100 to 800 with several inclination angles, α ranging from 5° to 75° by using BFS geometry to understand the characteristics of the flow field downstream of the vehicle geometry. In addition, the reattachment length was investigated at higher upstream lengths, u_l. The results showed that, u_l and α do not affect the reattachment length too much. In addition, vortex shedding was increased by a decrease of inclination angles, α at $\alpha < 15°$. Louda et al. (2013) carried out a computational investigation of flow through a BFS having various inclination angles, $\alpha = 10°, 25°, 45°$ and $90°$ at $\mathrm{Ho/Hi} = 2.25$ and at $Re_h = 15 \times 10^3$. They showed that inclination angle does not affect X_r except for $\alpha = 10°$. Prihoda et al. (2012) investigated the BFS geometry with inclination angles of α = 20°, 30° and 45° for H_o/H_i = 3 and $70 \times 10^3 < Re_h < 160 \times 10^3$ using PIV. They showed that the reattachment length was nearly the same for α = 30° and 45° whereas it significantly decreased for α = 20°, e.g., X_r/h = 3.4, 6.5, and 7.3 for α = 20°, 30° and 45°, respectively at $Re_h = 7{,}3 \times 10^4$. Choi et al. (2016) carried out a numerical investigation for different inclination angles from 10° to 90° and expansion ratios, Ho/Hi = 1.48, 2.00 and 3.27, and Reynolds numbers from Re = 5×10^3 to 64×10^3 by using RANS and LES turbulence models. The results showed that, reattachment length remains almost constant when the inclination angle, α was bigger than 30°. Singh et al. (2011) numerically investigated the effect of step angle, expansion ratio and Reynolds number on separation length in BFS geometry. The Re_h varied between 15×10^3 and 64×10^3, the analysed step angles include 15°, 30°, 45°, and 90°, while the expansion ratios examined are 1.48 and 2.0. The results showed that, the reattachment length was almost constant among the 45° - 90° inclination angles for all Re_h and expansion ratios. The X_r was decreased by reduce the inclined angle at $\alpha < 45°$. X_r is $3.78xh$ at 15° while it is $7.1xh$ at 90°. Wu et al. (2013) investigated the effect of the roughened wall, having two different roughness and placed upstream of BFS, on the characteristics of downstream separated flow for Re_h =3450 and H_o/H_i

=1.01 experimentally. They showed that the reattachment length was X_r/h = 4.25 for the normal smooth surface whereas the X_r/h reduced to 4.4 when the rough surface was placed far upstream of BFS. Additionally, the X_r/h was further reduced to 3.3 when the rough surface was placed closer to the BFS.

A number of active flow control systems, e.g., periodic perturbation by synthetic jet, zero or non-zero net mass flux by blowing and suction, and plasma actuators, were used in the previous studies to control the characteristics of the separated flow downstream of the BFS geometry (Okada et al., 2012; Uruba et al., 2007; D'Adamo et al., 2014; Benard et al., 2016). Periodic perturbation by a synthetic jet is the most used among them (Kang and Choi, 2002). Previous studies showed that the periodic perturbation reduced the reattachment length while the shear layer growth rate and the turbulence intensity were increased (Yoshioka et al.; 2001 a,b, Hasan, 1992). Thus, the increase in Reynolds stress enhanced the momentum transfer across the shear layer, urging the separated flow to reattach. In fact, it was shown that the reattachment length is inversely linear proportional to the total rate of the momentum entrainment, via increasing the total circulation, to the separated flow downstream of a BFS (Berk et al., 2017). Additionally, increasing the Strouhal number decreases the total circulation of the flow.

The synthetic jet actuator, located at the top corner of the step, was used in the experimental study by Li et al. (2020) to investigate the characteristics of a turbulent-separated flow downstream of a BFS at Re_h = 9630. They observed that the location of the reattachment position was changed for different perturbation frequencies and amplitudes. Therefore, there should be an optimum frequency for the periodic perturbation assisting the flow to reattach at downstream of a BFS. (Yoshioka et al., 2001 a,b). In the study of Dejoan and Leschziner (2004), a perturbation frequency at the Strouhal number of 0.2 caused the largest reduction of the time-averaged recirculation length. Similarly, Yoshioka et al. (2001 a,b) showed a 30% reduction of the reattachment length when using an optimum frequency of St = 0.19. Additionally, Okada et al. (2012) used a synthetic jet with a non-dimensional frequency of 0.2, located before the step corner at Re_h = 5000. They found that the reattachment length was reduced by 20% when compared to the case without a jet. On the other hand, in the study of Xu et al. (2015), the optimum frequency was reported as somewhat smaller as St_h = 0.053 for the optimum jet slot angle of 127.5° and for Re_h = 40665. The critical frequency of the actuator was revealed as the characteristic frequency of the shear layer downstream of a BFS. Below the critical frequency, the actuator alters the characteristics of the shear layer remarkably whereas the effect of the actuator on the shear layer was weak above the critical frequency (Li et al., 2019).

Besides, Uruba et al. (2007) investigated the effects of suction and blowing on the characteristics of a flow downstream of a BFS by placing a slot at the bottom of a step. They revealed that the suction performance is not influenced by the slot geometry, whereas the blowing performance is influenced by the slot geometry. Mehrez et al. (2010) used periodic perturbation to control flow at a relatively higher Reynolds number, i.e., $Re_h = 3.3 \times 10^4$, by using suction and blowing through a slot located at the top edge of the step. Simulation was carried out at four different perturbation frequencies characterized by Strouhal number of St_h = 0, 0.05, 0.25, 1. The location of the reattachment point was measured at X_r/h = 7.2 for zero-perturbation frequency, *i.e.*, St_h = 0. The shortest reattachment length was obtained at Strouhal number of St_h = 0.25. Finally, Zhao and Dong (2020) found that the stabilizing effect of suction on the boundary layer flow increased with its flux. Zero net mass flow actuators, ensuring the total mass flow rate over a complete cycle is zero, were also effectively used in controlling the shear layer (Mushyam and Bergada, 2015). A slot jet with a zero net mass-flow rate was employed in many studies (Dejoan and Leschziner, 2004; Kang and Choi, 2002; Kapiris and Mathioulakis, 2014) . Suboptimal feedback control via varying blowing and suction with zero-net mass flow rate applied at the step edge by Kang and Choi (2002) to a flow over a BFS at Re_h = 5100 decreased the reattachment length greatly when compared to those of uncontrolled flow and flow with single-frequency actuation. The high sensitivity to the perturbation at the considered Strouhal number is due to a strong interaction between shear-layer instabilities, amplified by the perturbation, and shedding-type instabilities. These instabilities are induced by the interaction of large-scale structures developing downstream of the step with the wall, causing the shear layer to oscillate (Dejoan and Leschziner, 2004; Bouda et al., 2008). Furthermore, in the study of Kapiris and Mathioulakis (2014) conducted at Re_h=6940, pulsating jets of non-zero net mass flux emerging at the step edge with $0.026 < St_h < 0.23$ resulted in a 20% maximum reduction of the recirculation length. They showed that optimal periodic blowing produces vortical structures with higher circulation and fewer numbers compared to non-optimal and unforced scenarios.

Two types of shear layer instability, i.e., the “shear layer mode” of instability (at St_{θ}=0.012) and the “step mode” of instability (at St_{θ} = 0.185) was declared in the study of Hasan (1992) in which laminar separation under controlled perturbation for a Re_h=11000 was studied. As a result, Hasan (1992) reported the shear layer flapping with a low-frequency and shear layer splitting. In the study of Yoshioka et al. (2001 a,b), the flow over a BFS at Re = 3700 was perturbed with three perturbation frequencies, e.g., St_h = 0.08, 0.19, 0.30, from the step edge to clarify the interaction between the developed vortices with the downstream separated flow. They found that the perturbation frequencies below or equal to the optimized perturbation frequency were able to produce strong enough vortices that developed the regions of large Reynolds stress to change the mean velocity field.

Three regimes of Strouhal number, i.e., low, intermediate, and high Strouhal numbers, were identified by Berk et al. (2017) in which the periodic forcing of the flow over a BFS at Re_h = 41000 for a range of 0.21 < St_H < 1.98 was investigated. As a result, in a low-Strouhal-number regime, vortices develop at a late stage relative to the recirculation region, leading to reduced effectiveness. At high Strouhal numbers, vortices either re-enter the actuator or are packed so closely that they cancel each other out, both of which diminish the forcing effectiveness. In the intermediate regime, a vortex train forms, and the circulation decay intensifies with higher Strouhal numbers of which provides an explanation for the variations observed in reattachment length. A similar study, which investigated the effect of forcing frequency range between 0.036 $\leqslant St_h \leqslant$ 1.98, was conducted by McQueen et al. (2022) at relatively higher Reynolds numbers, i.e., $1.18 \times 10^5 \leqslant Re_h \leqslant 4.72 \times 10^5$. They achieved to perturb the shear layer despite the high Reynolds number. McQueen et al. (2022) further elaborated on the relation between the separated flow downstream of the BFS and forcing frequency. They reported that the perturbation frequency, which was close to the shear layer instability, not only reduced the reattachment length, X_r, but also reduced the base pressure, i.e., reduction up to 45% when compared to non-perturbed case. On the other hand, perturbation with a higher frequency caused an increase in both mean base pressure and reattachment length because more flow entrained upstream to the step-base due to the reduced initial growth of the shear-layer instability and stabilized latter half of the reattachment zone. Finally, Chovet et al. (2019) used a sinusoidal actuator with St_h, from 0.045 to 0.453 to control the flow characteristics downstream of a BFS at Re_h = 30450. Results indicate that an excitation at St_h = 0.226, linked to the shedding frequency, leads to a decrease of the external reattachment length.

A Coanda actuator is a device that blows a fluid through a slot to control the characteristics of a downstream flow. The Coanda effect is generated using a circulation control surface placed next to a blowing slot. A Coanda actuator does not need any moving control surfaces, which decreases the appendage weight, noise, and complexity of the method. Additionally, a Coanda actuator can respond to the of flow unsteadiness in a very short duration of time interval (Lubert, C., 2011). In the previous literature, Coanda actuators were mainly used in investigations to increase the lift of aerofoils since the late 1960s. For example, Jones et al. (2002) investigated the aerodynamics of a flap by using a Coanda actuator. There were two blowing slots that were upper surface blowing and lower surface blowing. The results of Jones et al. (2002) showed that while upper surface blowing increases the lift coefficient, lower surface blowing decreases the lift coefficient. Additionally, Coanda actuators were used on ground vehicles for blowing at different frequencies in different positions to reduce their drag coefficients (Pfeiffer and King, 2012; Manosalvas et al., 2015 and 2016; Geropp and Odenthal, 2000). In the studies of Pfeiffer and King (2012), Manosalvas et al. (2015 and 2016) and Geropp and Odenthal (2000), C_D of the vehicle models decreased by 22%, 18%, and 10%, respectively. Pfeiffer and King (2012) did the most effective study by positioning the actuators on the top edge and side edges of the vehicle. Furthermore, Barros et al. (2016) showed that the Coanda blowing increases the rear pressure of a square-back Ahmed body by about 30% with a high-frequency actuation. They also showed that the Coanda blowing decreased the wake width downstream of the square-back Ahmed body and the maximum magnitude of vorticity in the wake region by more than 15%. On the other hand, Coanda actuators have not been widely used to control the flow downstream of a BFS. Velikorodyny et al. (2010) created a Coanda flow by locating a jet at 2 mm upstream of the BFS. Velikorodyny et al. (2010) measured the length of the reattachment point as X_r/h = 2.7 in their experimental study of a BFS flow at Re_h = 3000. Unlike the other

Coanda studies, Velikorodyny et al. (2010) located the slot before the separation point of the flow which decreased the Coanda's blowing effect on the flow.

3. MATERIAL AND METHODS

In the present study, the characteristics of the separated and attached flow and its control were investigated numerically with the aid of the backward-facing step, BFS. In the investigations, different turbulence models, e.g., Spalart-Almaras, realizable k- ε and SST k-ω turbulence models, together with different flow control methods were employed, i.e., the Coanda actuator as the active flow control method and the inclined-double backward-facing step as the passive flow control.

3.1. The Flow Geometry

Two-dimensional backward-facing step geometry was used. The step height was 25 mm which gave an expansion ratio of $H_o/H_i = 1.08$. Three different Reynolds numbers were used, e.g., $Re_h = 6 \times 10^3, 9.6 \times 10^3, 20 \times 10^3$, based on the step height, h, and free stream velocity, U_∞. All details of the flow geometry including the Coanda actuator are given in Figure 3.1.

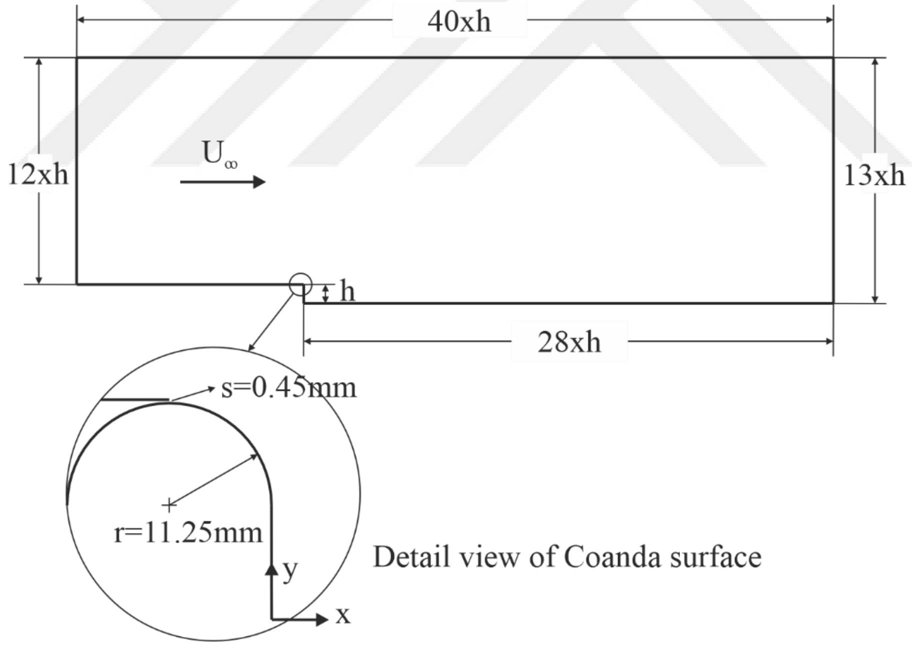

Figure 3.1. The geometrical details of the backward-facing step with the Coanda actuator.

The Coanda actuator was located at the top corner of the backward-facing step as shown in Figure 3.1. The geometrical details of the Coanda actuator were defined by using the study of Englar (1971). Thus, the height of the Coanda exit, s, and the radius of the Coanda surface, r, were found to be s = 0.45 mm and r = 11.25 mm, respectively. The details are found to be in

Appendix 1. Additionally, the momentum coefficient, C_M, which was used to define the jet velocity at the Coanda exit is given in Equation (3.1.1).

$$C_M = \frac{\dot{m}U_j}{\frac{1}{2}\rho U_\infty^2 A_h} \tag{3.1.1}$$

In Equation (3.1.1), U_j was the jet velocity at the Coanda exit, $\dot{m}$ was the mass flow rate at the Coanda exit, U_∞ was the free stream velocity, and A_h was the cross-sectional area of the channel. The jet velocity at the Coanda exit, U_j, was determined based on the range of momentum coefficient $0.02 \leq C_M \leq 0.14$ and Reynolds number range of $\mathrm{Re}_h = 6 \times 10^3, 9.6 \times 10^3, 20 \times 10^3$.

3.2. The Governing Equations of the Flow

The flow through the BFS was solved using a two-dimensional and incompressible continuity and Navier-Stokes equations as shown in Equations (3.2.1) and (3.2.2).

$$\frac{\partial u_i}{\partial x_i} = 0 \tag{3.2.1}$$

$$\rho \left[\frac{\partial u_j}{\partial t} + u_i \frac{\partial u_j}{\partial x_i}\right] = -\frac{\partial P}{\partial x_j} + \mu \frac{\partial^2 u_j}{\partial x_i^2} + \rho g_j \tag{3.2.2}$$

Unsteady flow variables, density, ρ, velocities, u_j, are defined as follows

$$\rho = \bar{\rho} \quad \text{and} \quad \rho' = 0, \quad u_j = \bar{u}_j + \acute{u}_j, P = \bar{P} + P' \tag{3.2.3}$$

Putting the abovementioned definitions of the flow parameters, given in the Equation (3.2.3), in the Navier-Stokes equation, given in (3.2.2), gives the Reynolds equation as shown in Equation (3.2.4)

$$\bar{\rho}\bar{u}_i \left[\frac{\partial \bar{u}_j}{\partial x_i}\right] = -\frac{\partial \bar{P}}{\partial x_j} + \frac{\partial}{\partial x_i}\left[\mu \frac{\partial \bar{u}_j}{\partial x_i} - \bar{\rho}\overline{u'_i u'_j}\right] + \bar{\rho} g_j \tag{3.2.4}$$

Boussinesq approximation equates the transport of turbulent velocity fluctuations to the molecular momentum transport in an isotropic Newtonian fluid as shown in Equation (3.2.5).

$$\bar{\rho}\overline{u'_i u'_j} = -\bar{\rho}\nu_T\left(\frac{\partial \bar{u}_j}{\partial x_i} + \frac{\partial \bar{u}_i}{\partial x_j}\right) \tag{3.2.5}$$

3.2.1. Spalart Allmaras Turbulence Model

The Spalart-Allmaras turbulence model is a single-equation model utilized for solving a formulated transport equation governing the kinematic eddy viscosity. In general, the Spalart-Almaras turbulence model is used for flow that involve boundary layers subjected to adverse pressure gradients. The transported variable defined in the Spalart-Almaras turbulence model, $\tilde{v}$, is the same with the turbulent kinematic viscosity except in the near-wall region. The transport equation for $\tilde{v}$ is

$$\frac{\partial}{\partial t}(\rho\tilde{v}) + \frac{\partial}{\partial x_i}(\rho\tilde{v}u_i) = G_v + \frac{1}{\sigma_{\tilde{v}}}\left[\frac{\partial}{\partial x_j}\left\{(\mu + \rho\tilde{v})\frac{\partial \tilde{v}}{\partial x_j}\right\} + c_{b2}\rho\left(\frac{\partial \tilde{v}}{\partial x_j}\right)^2\right] - Y_v + S_{\tilde{v}} \tag{3.2.6}$$

where Y_v is the destruction of turbulent viscosity in the near-wall region and G_v is the production of turbulent viscosity, c_{b2} and $\sigma_{\tilde{v}}$ are the constants and v is the molecular kinematic viscosity.

The turbulent viscosity, is computed from

$$\mu_t = \rho\tilde{v}f_{v1} \tag{3.2.7}$$

where the viscous damping function, f_{v1}, is given by

$$f_{v1} = \frac{\chi^3}{\chi^3 + C_{v1}^3} \tag{3.2.8}$$

and

$$\chi \equiv \frac{\tilde{v}}{v} \tag{3.2.9}$$

The production term, G_v, is modelled as

$$G_v = c_{b1}\rho\tilde{S}\tilde{v} \tag{3.2.10}$$

where

$$\tilde{S} \equiv S' + \frac{\tilde{v}}{\kappa^2 + d^2} f_{v2} \tag{3.2.11}$$

And

$$f_{v2} = 1 - \frac{\chi}{1 + \chi f_{v1}} \tag{3.2.12}$$

c_{b1} and κ are constants, while d denotes the distance from the wall, and S' serves as a scalar indication of the deformation tensor. S' is based on the magnitude of the vorticity.

$$S' \equiv \sqrt{2\Omega_{ij}\Omega_{ij}} \tag{3.2.13}$$

Where Ω_{ij} is the mean rate-of-rotation tensor and is defined by

$$\Omega_{ij} = \frac{1}{2}\left(\frac{\partial u_i}{\partial x_j} - \frac{\partial u_j}{\partial x_i}\right) \tag{3.2.14}$$

3.2.2. SST *k-ω* Turbulence Model

Menter (1994) introduced the SST k-ω turbulence model, aiming to combine the strengths of both k-ε and k-ω models within the Shear-Stress Transport (SST). By integrating the near-wall precision of the k-ω model with the far-field insensitivity to free-stream conditions characteristic of the *k-ε* model, the SST model achieves a balanced performance across varying flow regimes. *k*-ω SST turbulence model is most widely used models in aerodynamic flows and it is better to solve separation flows. The transport equations in the SST k-ω model appear in Equations (5) and (6) as follows;

$$\frac{\partial}{\partial t}(\rho k)+\frac{\partial}{\partial x_i}(\rho k u_i)=\frac{\partial}{\partial x_j}\left[\Gamma_k\frac{\partial k}{\partial x_j}\right]+G_k-Y_k+S_k \tag{3.2.15}$$

and

$$\frac{\partial}{\partial t}(\rho\omega)+\frac{\partial}{\partial x_j}(\rho\omega u_j)=\frac{\partial}{\partial x_j}\left[\Gamma_\omega\frac{\partial \omega}{\partial x_j}\right]+G_\omega-Y_\omega+D_\omega+S_\omega \tag{3.2.16}$$

G_k and G_ω represents the production of turbulent kinetic energy, k, and ω, respectively and given by.

$$G_\omega=\frac{\alpha}{v_t}G_k \tag{3.2.17}$$

Y_k and Y_ω represents the dissipation of turbulent kinetic energy, k and ω, respectively and given by.

$$Y_k=\rho\beta^*k\omega \tag{3.2.18}$$

$$Y_\omega=\rho\beta\omega^2 \tag{3.2.19}$$

β_i is calculated as

$$\beta_i=F_1\beta_{i,1}+(1-F_1)\beta_{i,2} \tag{3.2.20}$$

Γ_k and Γ_ω represent the effective diffusivity of k and ω, respectively and given by

$$\Gamma_k = \mu + \frac{\mu_t}{\sigma_k} \tag{3.2.21}$$

and

$$\Gamma_\omega = \mu + \frac{\mu_t}{\sigma_\omega} \tag{3.2.22}$$

Where σ_k and σ_w are the Prandtl numbers for k and ω, respectively. μ_t is the turbulent viscosity that calculated as described below

$$\mu_t = \frac{\rho k}{\omega}\frac{1}{max\left[\frac{1}{a^*},\frac{SF_2}{a_1\omega}\right]} \tag{3.2.23}$$

where S is the strain rate magnitude and

$$\sigma_k = \frac{1}{\frac{F_1}{\sigma_{k,1}} + (1-F_1)/\sigma_{k,2}} \tag{3.2.24}$$

$$\sigma_\omega = \frac{1}{\frac{F_1}{\sigma_{\omega,1}} + (1-F_1)/\sigma_{\omega,2}} \tag{3.2.25}$$

Blending functions, F_1 and F_2, are given by

$$F_1 = \tanh(\emptyset_1^4) \tag{3.2.26}$$

$$\emptyset_1 = min\left[max\left(\frac{\sqrt{k}}{0.09\omega y},\frac{500\mu}{\rho y^2\omega}\right),\frac{4\rho k}{\sigma_{\omega,2}D_\omega^+ y^2}\right] \tag{3.2.27}$$

$$D_\omega^+ = \max\,[2\rho\frac{1}{\sigma_{\omega,2}}\frac{1}{\omega}\frac{\partial k}{\partial x_j},10^{-10}] \tag{3.2.28}$$

$$F_1 = \tanh(\emptyset_2^2) \tag{3.2.29}$$

(3.2.30)

$$\emptyset_2 = max\left[2\frac{\sqrt{k}}{0.09\omega y}, \frac{500\mu}{\rho y^2\omega}\right]$$

where y is the distance to next surface and D_ω^+ is the positive portion of the cross-diffusion term. Some constants in equations are given by

$\sigma_{k,1}$	$\sigma_{\omega,1}$	$\sigma_{k,2}$	$\sigma_{\omega,2}$	a_1	$\beta_{i,1}$	$\beta_{i,1}$
1.176	2.0	1.0	1.168	0.31	0.075	0.0828

3.2.3. Realizable k-ε Turbulence Model

The most important feature that distinguishes it from standard *k*-*ε* is the realizable *k*- *ε* model contains an alternative formulation for the turbulent viscosity. This turbulence model widely used in free flows including jets and mixing layers, separated flows and boundary layer flows.

The transport equation of k;

$$\frac{\partial}{\partial t}(\rho k) + \frac{\partial}{\partial x_j}(\rho k u_j) = \frac{\partial}{\partial x_j}\left[\left(\mu + \frac{\mu_t}{\sigma_k}\right)\frac{\partial k}{\partial x_j}\right] + G_k + G_b - \rho\varepsilon - Y_M + S_k \qquad (3.2.31)$$

The transport equation of ε;

$$\frac{\partial}{\partial t}(\rho\varepsilon) + \frac{\partial}{\partial x_j}(\rho\varepsilon u_j) = \frac{\partial}{\partial x_j}\left[\left(\mu + \frac{\mu_t}{\sigma_\varepsilon}\right)\frac{\partial\varepsilon}{\partial x_j}\right] + \rho C_1 S_\varepsilon - \rho C_2\frac{\varepsilon^2}{k + \sqrt{v\varepsilon}} + C_{1\varepsilon}\frac{\varepsilon}{k}C_{3\varepsilon}G_b + S_\varepsilon \qquad (3.2.32)$$

where

$$C_1 = max\left[0.43, \frac{\eta}{\eta + 5}\right] \qquad (3.2.33)$$

$$\eta = S\frac{k}{\varepsilon} \qquad (3.2.34)$$

$$S = \sqrt{2S_{ij}S_{ij}} \tag{3.2.35}$$

In this equation, G_k, represents the generation of turbulence kinetic energy resulting from mean velocity gradients. G_b is the generation of turbulence kinetic energy due to buoyancy. Y_M denotes the role of fluctuating dilatation in compressible turbulence, contributing to the total dissipation rate. σ_k and σ_ε are the turbulent Prandtl numbers for k and ε. S_k and S_ε are user-defined source term. C_2 and $C_{1\varepsilon}$ are constant.

The eddy viscosity is computed from

$$\mu_t = \rho C_{\mu 1} \frac{k^2}{\varepsilon} \tag{3.2.36}$$

C_μ is not constant and it is computed from

$$C_\mu = \frac{1}{A_0 + A_s \frac{kU^*}{\varepsilon}} \tag{3.2.37}$$

where

$$U^* = \sqrt{S_{ij}S_{ij} + \tilde{\Omega}_{ij}\tilde{\Omega}_{ij}} \tag{3.2.38}$$

And

$$\tilde{\Omega}_{ij} = \Omega_{ij} - 2\varepsilon_{ijk}\omega_k \tag{3.2.39}$$

$$\Omega_{ij} = \overline{\Omega}_{ij} - \varepsilon_{ijk}\omega_k \tag{3.2.40}$$

Here, $\overline{\Omega}_{ij}$ represents the mean rate-of-rotation tensor observed from a moving reference frame with angular velocity ω_k. The values of model constants A_0 and A_s are as follows:

$\boldsymbol{A_0}$	$\boldsymbol{A_s}$

$\mathbf{4.04}$	$\sqrt{6}\cos\emptyset$

where

$$\emptyset = \frac{1}{3}\cos^{-1}\left(\sqrt{6}W\right) \tag{3.2.41}$$

$$W = \frac{S_{ij}S_{jk}S_{ki}}{\tilde{S}^3} \tag{3.2.42}$$

$$\tilde{S} = \sqrt{S_{ij}S_{ij}} \tag{3.2.43}$$

$$S_{ij} = \frac{1}{2}\left(\frac{\partial u_j}{\partial x_i} + \frac{\partial u_i}{\partial x_j}\right) \tag{3.2.44}$$

The model constants are

$C_{1\varepsilon}$	C_2	σ_k	σ_ε
$\mathbf{1.44}$	1.9	1	1.2

The governing equations of the flow was discretized and solved using a commercial CFD solver, Ansys Fluent. SIMPLEC solution algorithm was used to solve the velocity-pressure coupled equation. Least squares Cell Based was used to calculate the gradient of the flow variables. The Quick scheme was used for the convective discretization of the governing equations.

3.3. The Boundary Conditions of the Computational Flow Domain

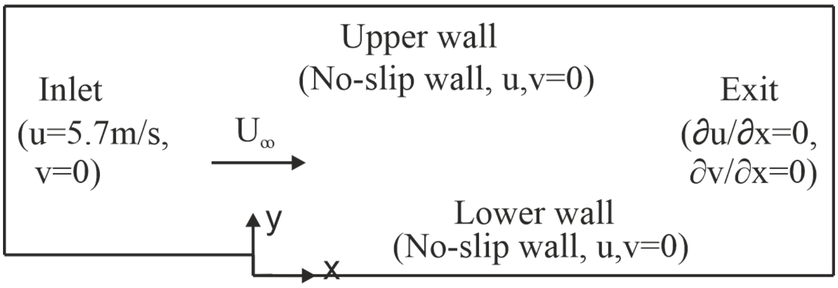

Figure 3.2. Boundary conditions of the computational flow domain including the backward-facing step.

The boundary conditions of the computational flow domain including the BFS were described in Figure 3.2. In total, the flow domain included three different boundary conditions as shown in Figure 3.2, namely, inlet, outlet, and wall boundary conditions. A uniform velocity profile perpendicular to the surface was defined at the main inlet to the flow domain. The second inlet boundary surface was located inside the Coanda surface at the corner of the step. The turbulence intensity was set to 1% at both inlet boundaries. Additionally, a zero velocity gradient was defined at the outlet boundary. Finally, a no-slip velocity boundary condition was used on the walls of the flow domain.

3.4. The Details of the Computational Mesh and Its Verification

Three meshes, named coarse, medium, and fine meshes, were generated in order to search for the most suitable mesh that did not affect the numerical solution. In the mesh independency study, the mesh that had the least number of nodes was named as the coarse mesh while the mesh that had the largest number of nodes was named as the fine mesh. The profile of the pressure coefficient, C_p, was chosen to check the suitability of the meshes. Figure 3.4 showed the distribution of the pressure coefficient, C_p, on the lower surface of the channel downstream of the step for three different turbulence models, which were obtained from three different meshes.

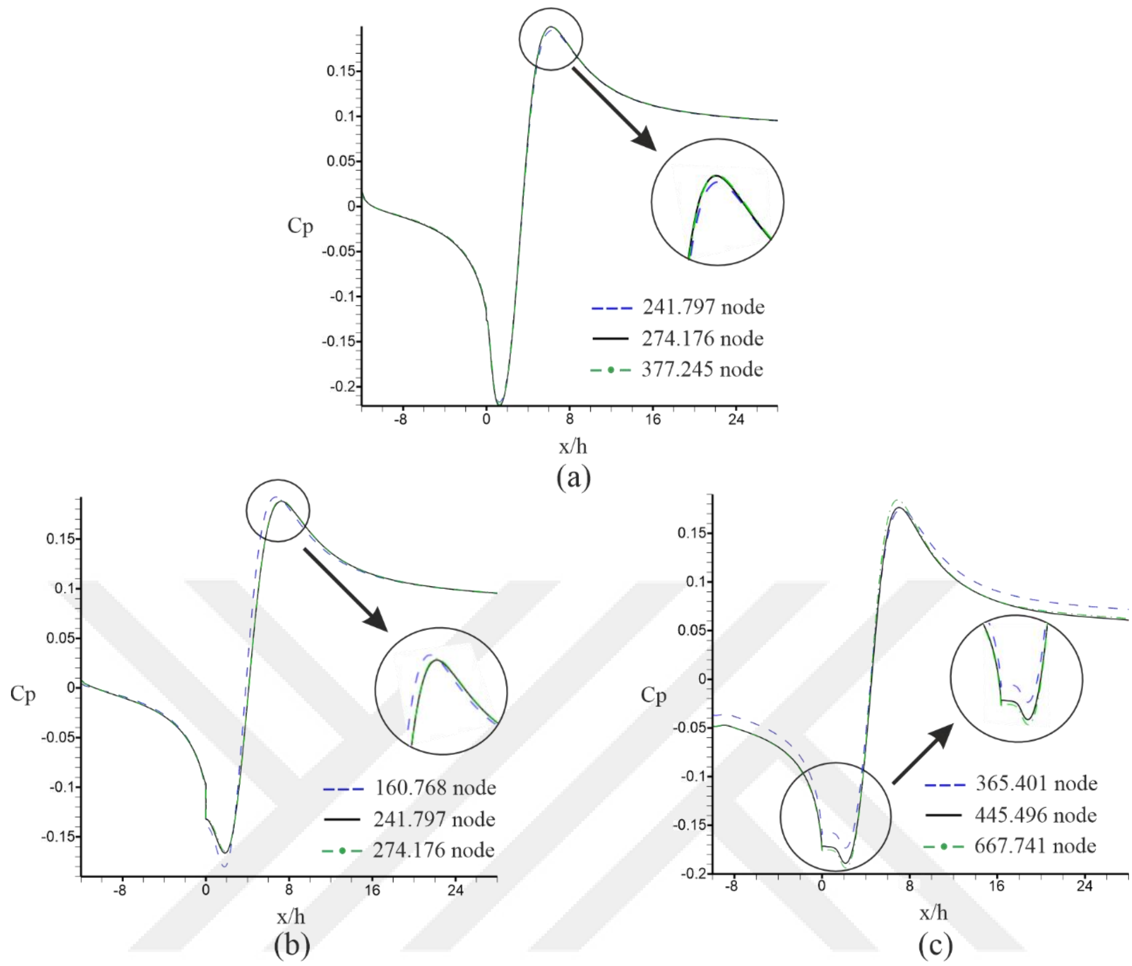

Figure 3.3. Pressure coefficient, C_p, results of three mesh for a. Spalart-Allmaras model, b. Realizable k-ε model c. SST k-ω model

Figure 3.3 presents that the results obtained by medium and fine meshes of all turbulence models showed good agreement with each other. Thus, the medium mesh was used in the present study, which can ensure an accurate result and save computational resources. Additionally, the maximum amount of the dimensionless wall thickness, y^+ of the meshes used in the mesh independence study, and their reattachment results are given in Table 3.1.

Table 3.1. The maximum amount of the dimensionless wall thickness, y^+, of the meshes that were used in the mesh independency study and their reattachment results.

Turbulence Model	Total Number of nodes	y+	X_r/h
Spalart Allmaras	241.797	44	4.35
	274.176	44	4.16
	377.245	50	4.28
Realizable k-ε	160.768	57	4.5
	241.797	40	5
	274.176	40	4.8
SST k-ω	365.401	1.58	5.44
	445.496	0.94	5.6
	667.741	0.94	5.44

The dimensionless wall thickness, y^+, results given in Table 3.1 show that the boundary layer meshes used for the meshes had the desired properties as the turbulence models used with them required. Additionally, the views of the meshes, which both involved and did not involve a boundary layer mesh on the walls of the channel, are presented in Figure 3.4.

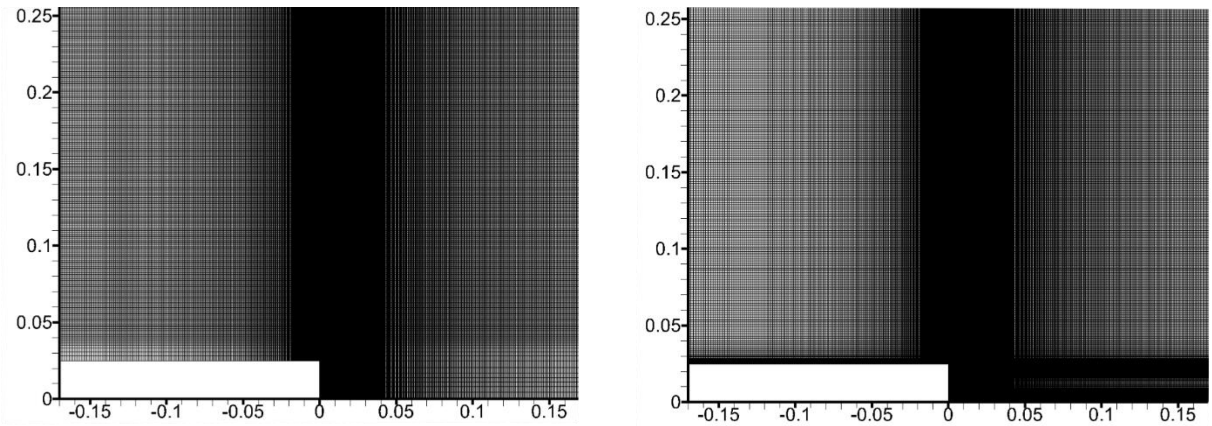

(a) (b)

Figure 3.4. a. Mesh with coarse boundary layer and b. Mesh with fine boundary layer.

4. RESULTS AND DISCUSSION

The results of the study are presented in two parts, and they are discussed in detail in this section of the thesis. In the first part, different RANS-based turbulence models, e.g., realizable k-ε, Spalart-Almaras and SST k-ω, were employed in order to evaluate their performance in the solution of the flow through a backward-facing step (BFS). In the second part, two different flow control methods, i.e., a Coanda actuator as an active flow control method and an inclined double backward facing step (DBFS) as a passive flow control method, were employed to control the characteristics of the wake flow downstream of the BFS.

4.1. Assessment of the Results of Different Turbulence Models

The results of the solutions of the flow through the BFS obtained by using Spalart Allmaras, realizable k-ε, and SST k-ω turbulence models are given as follows. In this part of the study, the traditional backward-facing step geometry, i.e., no-inclination angle, with the Reynolds number of the flow, $Re_h = 9.6 \times 10^3$, and the expansion ratio of the channel, H_o/H_i =1.08 were used.

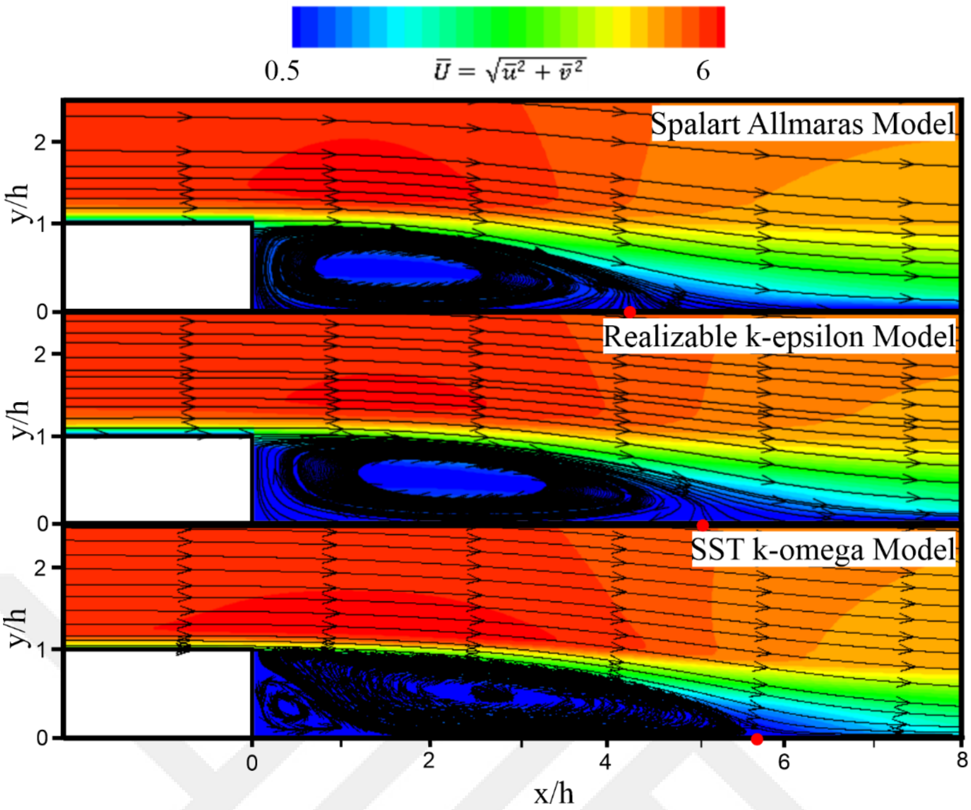

Figure 4.1. Time-averaged streamlines, $\bar{\psi}$, and velocity magnitude $\overline{U}=\sqrt{\bar{u}^2+\bar{v}^2}$, contours obtained by using different turbulence models.

Comparison of the time-averaged streamlines, $\bar{\psi}$, and velocity magnitude, $\overline{U}=\sqrt{\bar{u}^2+\bar{v}^2}$, contours obtained by using different turbulence models are given Figure 4.1. Additionally, the location of the reattachment point downstream of the BFS is shown with a red dot on each figure. Recirculation region which was formed as the result of flow separation at the top corner of the step was captured by all three turbulence models. However, the pattern and size of the recirculation regions captured by the turbulence models showed differences. For example, two focus points, F_1 and F_2, were captured as the result of SST k-ω turbulence model whereas only one focus point, F_1, was captured by Spalart-Almaras and realizable k-ε turbulence models. The occurrence of the secondary small recirculation region with focus F_2, forming near the lower step corner, was also verified in the experimental study of Li et al. (2020). The reattachment length was found as $X_r/h = 5.60$, 5.00 and 4.16 by the SST k-ω, the realizable k-ε and the Spalart-Allmaras models, respectively. Additionally, the reattachment length reported in the experimental study of Li et al. (2020), conducted for the same flow condition, was reported as

$X_r/h = 4.2$. Therefore, there are 28.5%, 17.0% and 0.95% differences between the results of the SST *k-ω*, the realizable k-ε, the Spalart-Allmaras models and the experimental result of Li et al. (2020). Thus, the result of the the Spalart-Allmaras model provided the best estimation among the turbulence models, that were employed in the present study, i.e., SST k-ω model and realizable k-ε model, with the experimental study of Li et al. (2020). A similar result was found in the study of Al-Jelawy et al. (2016).

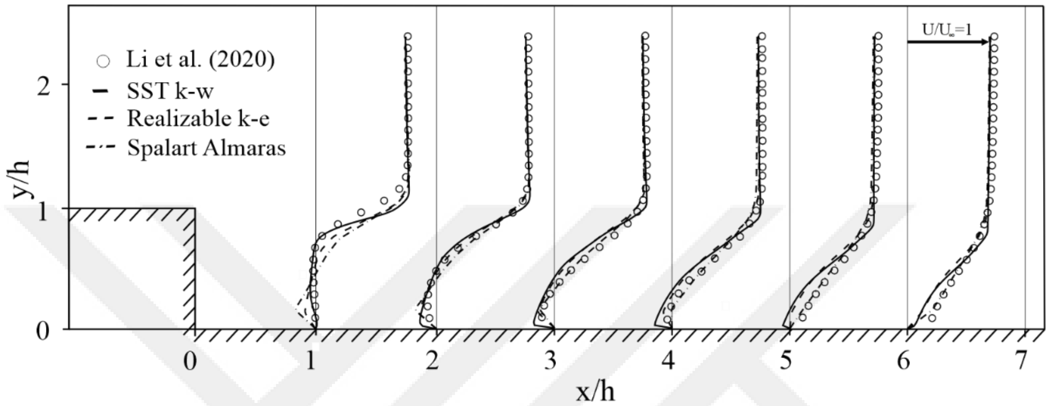

Figure 4.2. Profiles of the time-averaged streamwise velocity component normalized with the free stream velocity, $\bar{u}/U_\infty$

Comparisons of the time-averaged streamwise velocity component normalized with the free stream velocity, $\bar{u}/U_\infty$, results obtained by using different turbulence models with the experimental results of Li et al. (2020) are given in Figure 4.2. In general, the velocity profile results of turbulence models showed good agreement with the experimental results of Li et al. (2000) except at locations close to the wall and around the shear layer. In the recirculation region at which the streamwise velocity component results of all turbulence models had negative values, i.e., around $x/h < 5$, showed varying maximum velocity magnitudes. Thus, in the recirculation region, the maximum difference of 191 % with the experimental results of Li et al. (2020) was in the results of Spalart-Allmaras at $x/h = 1$. On the other hand, as seen in Figure 4.2, the velocity profiles of SST k-ω and Li et al. (2020) at locations between $x/h = 1$ and 3, showed good agreement. Thus, the maximum difference of 5% between the results of SST k-ω and Li et al. (2020) in this region showed good conformity between them. Besides, in the shear layer region, the maximum difference of 42% with the experimental results of Li et al. (2020) was in the results of the ST k-ω model at $x/h = 1$. Moreover, at the locations around

$x/h \geq 5$, i.e., after the reattachment point, at which the boundary layer redeveloped due to the wall effects, the maximum difference of 61% with the experimental results of Li et al. (2020) was in the results of SST k-ω at $x/h = 6$. Overall, it can be concluded that the conformity between the results of Spalart-Almaras and Li et al. (2020) was good in both the hear layer and after the reattachment point while the conformity between the results of SST k-ω and Li et al. (2020) was good in the recirculation region. The resolution of the secondary recirculation region, given in Figure 4.1, by SST k-ω turbulence can be explained with this good conformity between its results and the experimental results of Li et al. (2020) in the recirculation region. Additionally, the results of the realizable k-ε model were worse than the results of other turbulence models, i.e., SST k-ω and Spalart-Almaras, by not approaching the experimental results of Li et al. (2020) more than the other turbulence models in any regions of the flow.

In the next part of the study, the aim was to investigate the effectiveness of the flow control methods in controlling the characteristics of the separated flow downstream of the BFS. In line with this aim, the main target was to get the reattachment length of the recirculation region smaller. As explained above, the Spalart-Almaras model estimated the value of reattachment length with an error of 0.95% when compared with the experimental results. Thus, the Spalart-Almaras model was selected to be used for the next part of the study.

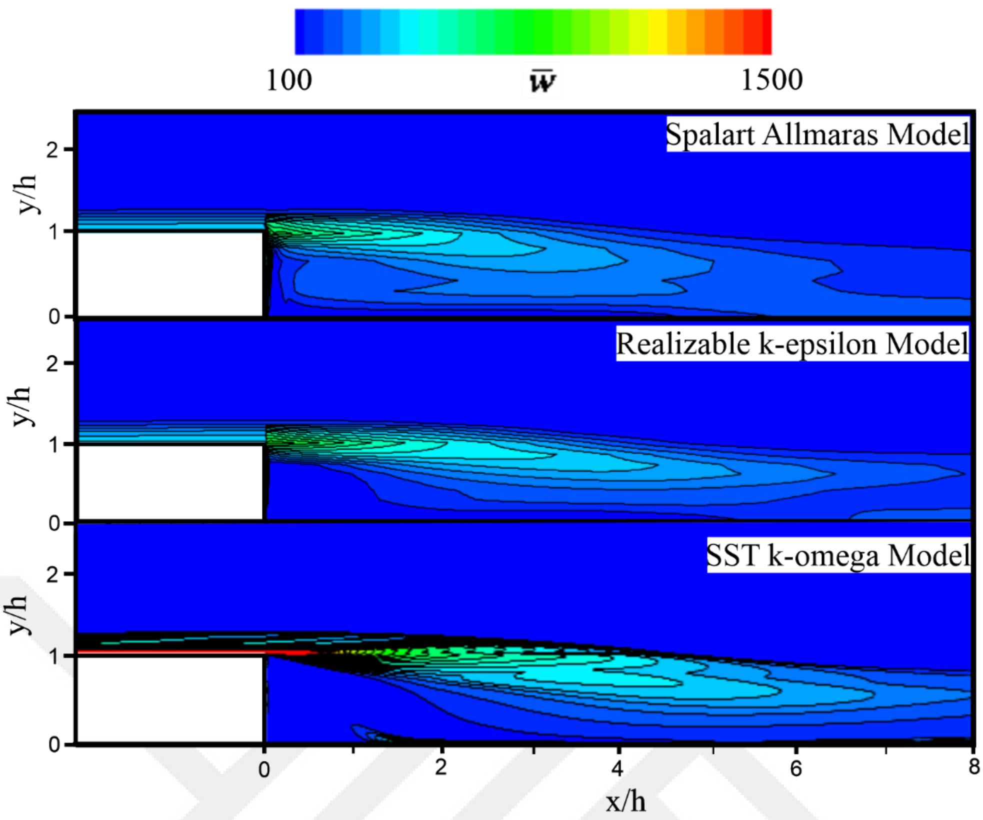

Figure 4.3. Time-averaged vorticity, $\overline{\omega}$, contours obtained by using different turbulence models.

The comparison of the time-averaged vorticity, $\overline{\omega}$, results obtained by using different turbulence models are given in Figure 4.3. The general pattern of the vorticity contour as the results of different turbulence models were similar, i.e., they were concentrated around the attached boundary layer on the upper wall of the step and around the shear layer separated at the upper corner of the step. However, in line with the findings about the reattachment length given above, the estimation of the vorticity magnitude by the SST *k-ω* turbulence model gave the maximum amount at around the upper corner of the step when compared to the other turbulence models, i.e., realizable *k-ε* and Spalart-Alamaras turbulence models. Additionally, in both results of the realizable *k-ε* and the SST *k-ω* turbulence models, the vorticity contours spread further downstream when compared to the results of the Spalart-Allmaras model indicating increased turbulence and instability in the shear layer, and potentially delaying the reattachment point.

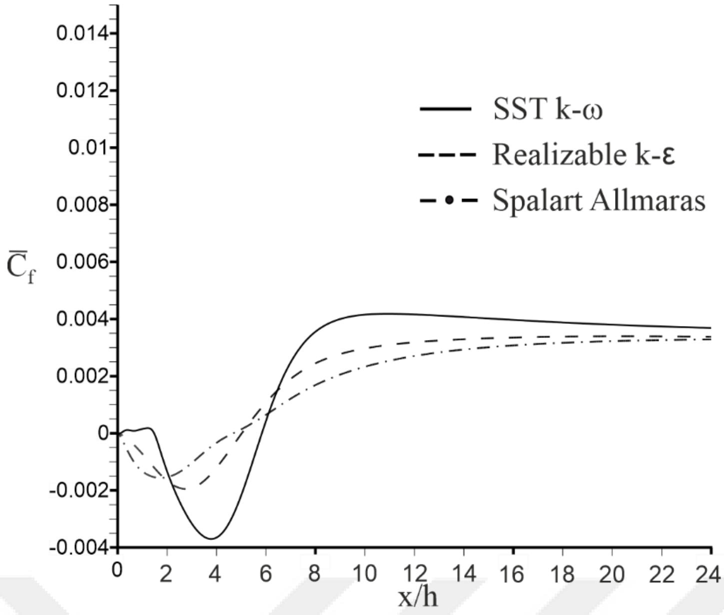

Figure 4.4. Time-averaged skin friction coefficient, $\bar{C}_f$, on the lower wall of the channel obtained by using different turbulence models.

The comparison of the time-averaged skin friction coefficient, $\bar{C}_f$, results on the lower wall of the channel obtained by using different turbulence models are given in Figure 4.4. The results given in Figure 4.4 show that the time-averaged skin friction coefficients, $\bar{C}_f$, had negative values due to the reversed flow in the recirculation region downstream of the BFS and their values continued to decrease to reach the minimum value in the recirculation region. After reaching the minimum value, they recovered towards the downstream flow direction. The similar trends for the $\bar{C}_f$ were seen in the results given in the previous studies (Al Jewaly et al., 2016; Khuwaranyu and Putivisutisa, 2009; Tihon et al., 2001). Although, the trends followed by the $\bar{C}_f$ results of all turbulence models were the same, their absolute maximums at extreme points were not the same. For example, the absolute maximums of $\bar{C}_f$ results of SST *k-ω* turbulence model were more than the results of realizable *k-ε* and Spalart-Almaras turbulence models both in the recirculation region and after the reattachment point. Additionally, the $\bar{C}_f$ profile on the lower wall of the channel might be useful in determining the reattachment point because at the reattachment point the value of the skin friction coefficient needs to be zero (Hu et al., 2020). Thus, as shown in Figure 4.4, the point at which the $\bar{C}_f = 0$ corresponds to *x*/*h* =

4.16, 5, 5.6 as the results of Spalart-Almaras, realizable k-ε and SST k-ω turbulence models, respectively, which are the same values of the reattachment points reported as above sections.

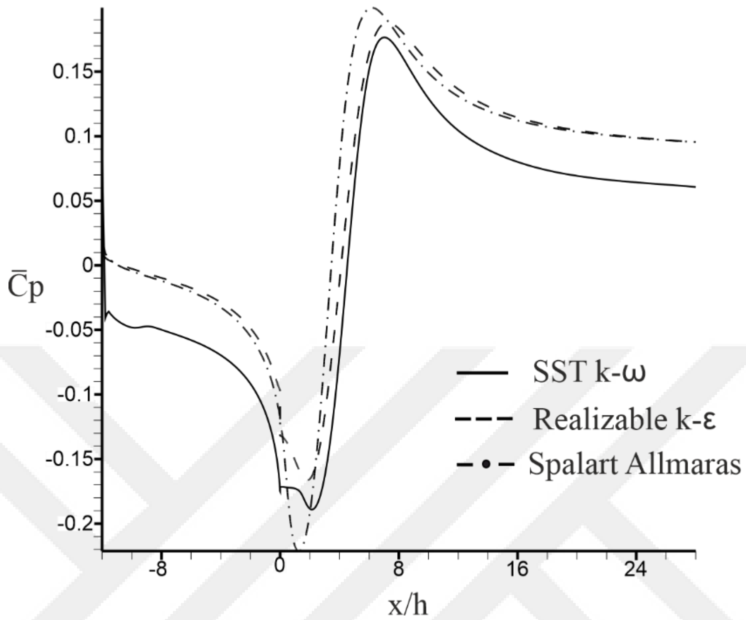

Figure 4.5. Time-averaged pressure coefficient, $\bar{C}_p$, on the lower wall of the channel obtained by using different turbulence models.

Comparison of the time-averaged pressure coefficient, $\bar{C}_p$, results on the lower wall of the channel obtained by using different turbulence models are given in Figure 4.5. The negative pressure coefficient near the step indicates a low-pressure region due to the flow separation. The pressure coefficient showed a similar trend as seen in previous studies (Kumar et al., 2020; Nakagawa and Nezu, 1987). Although $\bar{C}_p$ showed a similar decrease in the lower wall near the step for realizable k-ε and Spalart-Allmaras models, the decrease in $\bar{C}_p$ almost stopped between $0<x<0.05$ due to the secondary circulation region in the lower wall near the step for the SST k-ω turbulence model. Then, $\bar{C}_p$ gradually increased again in the downward flow. The $\bar{C}_p$ increased more sharply in the Spalart Allmaras model among the three models. Although, the agreement between realizable k-ε and Spalart-Allmaras models is good in the inlet of the channel, there was a difference after the step until the reattachment.

4.2 Application of Different Flow Control Methods

In this part of the study, the effectiveness of the flow control methods, including active and passive flow controls, was investigated. The Coanda actuator was used as the active flow control method and the inclined double backward-facing step was used as the passive flow control method.

4.2.1 The active flow control via the Coanda actuator

The geometric features of the Coanda actuator used in the present study were explained in detail in the section of 3.1. The Coanda actuator was placed at the top corner of the BFS. The aim was to investigate the effectiveness of the Coanda actuator in reducing the reattachment length, X_r that forms downstream of a BFS. Thus, three different Reynolds numbers were employed, i.e., $Re_h = 6 \times 10^3,\ 9.6 \times 10^3,$ and 20×10^3 in order to understand the effectiveness of the Coanda actuator at different free-stream velocities. Besides, four different momentum coefficients, $C_M = 0.02, 0.06, 0.10, 0.14$, were used that corresponded to different jet velocities at the Coanda actuator's blowing surface.

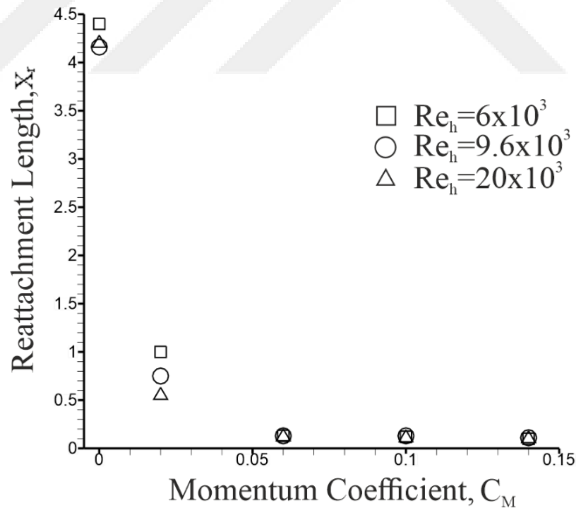

Figure 4.6. The reattachment length, X_r, with respect to the momentum coefficient, C_M , for different Reynolds numbers.

Figure 4.6 presents the change in the reattachment length, X_r, due to the application of the Coanda actuator at different Reynolds numbers, Re_h, and momentum coefficient, C_M. As shown in Figure 4.6, the reattachment length was around X_r/h = 4.4 at Reynolds numbers of Re_h =

6×10^3 and 9.6×10^3, the reattachment length slightly decreased to $X_r/h = 4.2$ as the Reynolds number was increased to 20×10^3. Inline with the findings, previous studies reported that the reattachment length increases linearly with the Reynolds number in the laminar regime and decreases or levels off in the turbulent regime (Armaly et al., 1983). Activating the Coanda actuator, at the momentum coefficient of $C_M = 0.02$, reduced the reattachment length drastically to $X_r/h = 1.0$, 0.58 and 0.56 for $Re_h = 6 \times 10^3$, 9.6×10^3, 20×10^3, respectively. Additionally, when the momentum coefficient of the blowing at the Coanda actuator was increased to C_M = 0.06, the reattachment points were further reduced to $X_r/h = 0.15$ for all Reynolds numbers tested. Further, increasing the momentum coefficient to $C_M = 0.1$ and 0.14 did not change the reattachment length. It can be concluded that the Coanda blowing at the momentum coefficient of $C_M = 0.02$ had slight differences for different Reynolds numbers while it had no differences for different Reynolds numbers at $C_M \geq 0.06$. Thus, there is no meaning to use the higher momentum coefficient than $C_M = 0.02$, i.e., an optimum momentum coefficient. Accordingly, the momentum coefficient of $C_M = 0.02$ was also reported as the most efficient and critical blowing coefficient for the flight characteristics of an airfoil by Pfeiffer and King (2014) and Manosolvas et al. (2016).

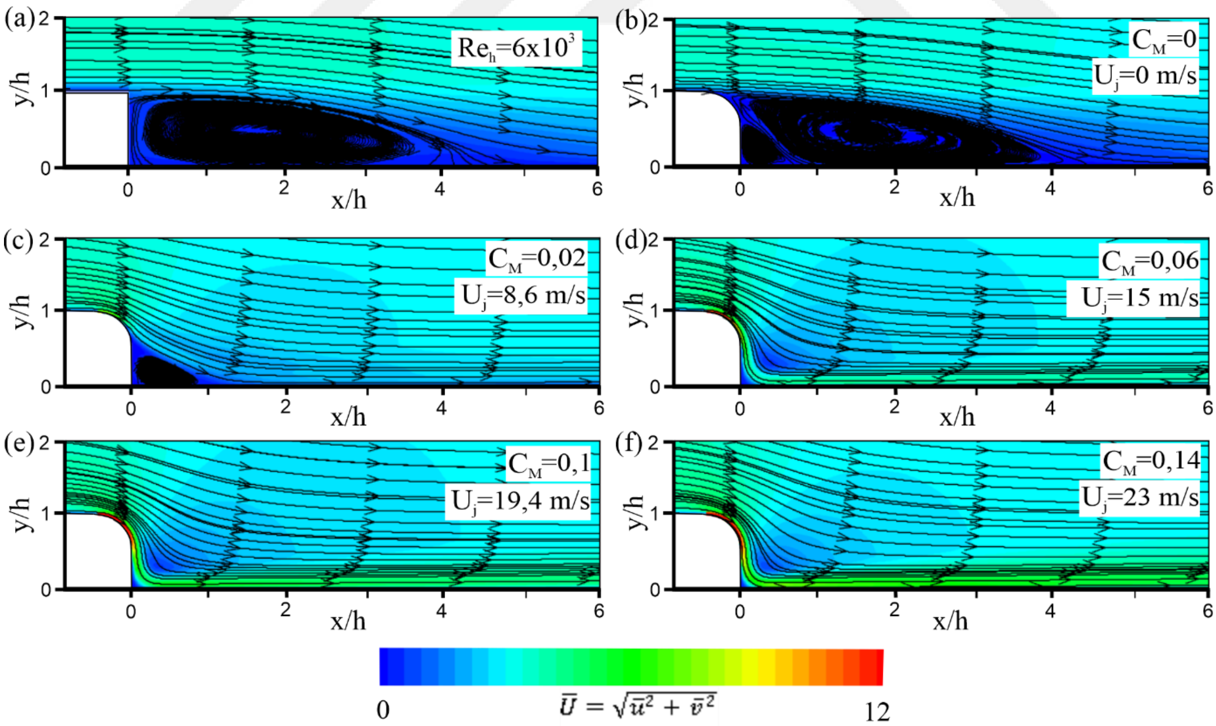

Figure 4.7. Time-averaged streamlines, $\bar{\psi}$, and velocity magnitude, $\bar{U} = \sqrt{\bar{u}^2 + \bar{v}^2}$, contours obtained with and without Coanda blowing for $Re_h = 6 \times 10^3$.

Comparison of the time-averaged streamlines, $\bar{\psi}$, and velocity magnitude, $\bar{U} = \sqrt{\bar{u}^2 + \bar{v}^2}$, contours obtained with and without the Coanda blowing for the Reynolds numbers of $\mathrm{Re}_h = 6 \times 10^3$, 9.6×10^3 and 20×10^3 are given in Figures 4.7, 4.8 and 4.9. As shown in Figure 4.7(a), the recirculation region that occurred downstream of the BFS for $\mathrm{Re}_h = 6 \times 10^3$ was similar to the one that occurred for $\mathrm{Re}_h = 9.6 \times 10^3$, e.g., the same reattachment point. On the other hand, modifying the top edge of the BFS to add the Coanda actuator changed the structure of the recirculation region in such a way that the occurrence of the secondary recirculation region at the bottom corner of the BFS, as shown in Figure 4.7(b). Additionally, modifying the BFS geometry by adding the Coanda actuator without a blowing caused an adverse effect of a slight increase in the reattachment length, i.e., the reattachment length, X_r, increased 2.7% when compared with the unmodified BFS geometry. The effects of the blowing through the Coanda actuator on the structure of the velocity field are presented in Figures 4.7(c)-4.7(f). The blowing at $C_M = 0.02$ using a Coanda actuator removed one of the recirculation regions and got the size of the recirculation drastically smaller. Moreover, the recirculation region dissipated completely at $C_M \geq 0.06$, instead a jet flow occurred that flow attached to the lower wall of the channel downstream of the BFS as the result of Coanda blowing. The jet flow became stronger as the momentum coefficient of the blowing was increased. Finally, at $C_M \geq 0.06$, a low velocity region formed over the jet flow when cornering that might indicate the over actuation of the Coanda actuator causing an adverse effect on the oncoming free stream flow.

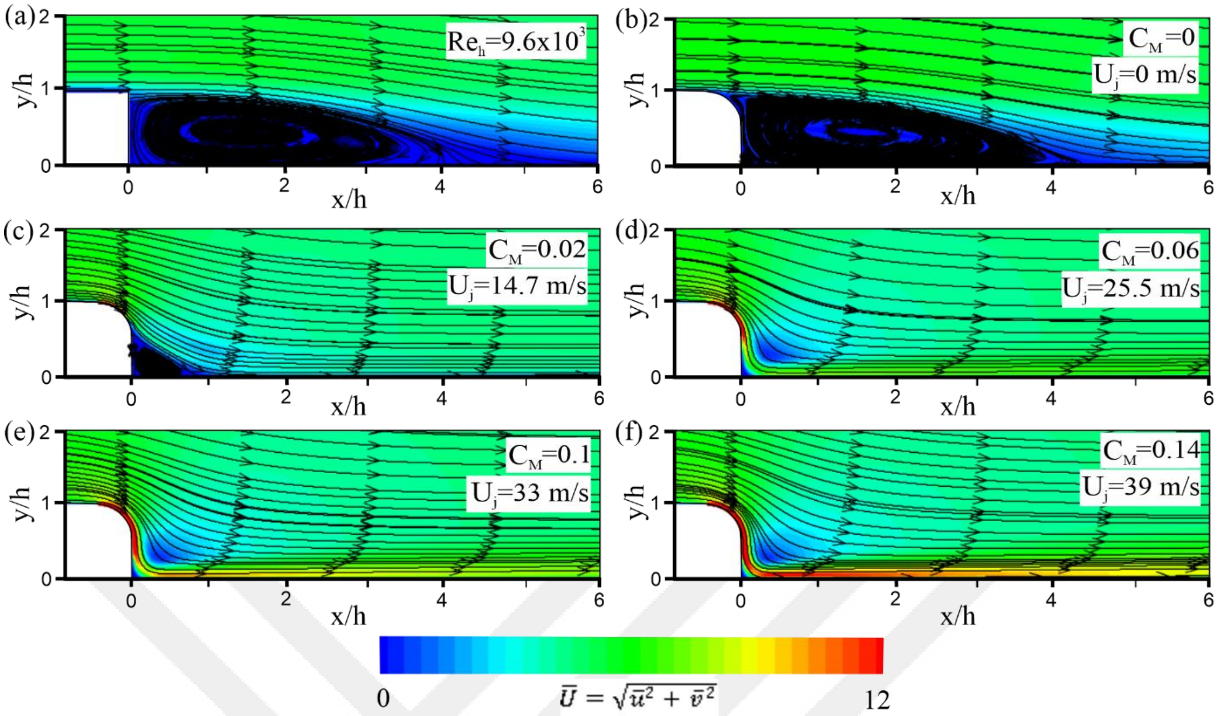

Figure 4.8. Time-averaged streamlines, $\bar{\psi}$, and velocity magnitude, $\bar{U} = \sqrt{\bar{u}^2 + \bar{v}^2}$, contours obtained with and without Coanda blowing for $Re_h = 9.6 \times 10^3$.

Figure 4.8 presents the structure of the velocity field when the Reynolds number of the flow increased to $\mathrm{Re}_h = 9.6 \times 10^3$. The characteristics of the velocity field, e.g., the geometry of the recirculation region, the jet flow, downstream of the BFS for $\mathrm{Re}_h = 9.6 \times 10^3$ were generally similar with the velocity field that occurred for $\mathrm{Re}_h = 6 \times 10^3$. The only differences were in the maximum magnitude of the flow velocity in all cases and the smaller size of the secondary recirculation region in case of the Coanda actuator with no blowing.

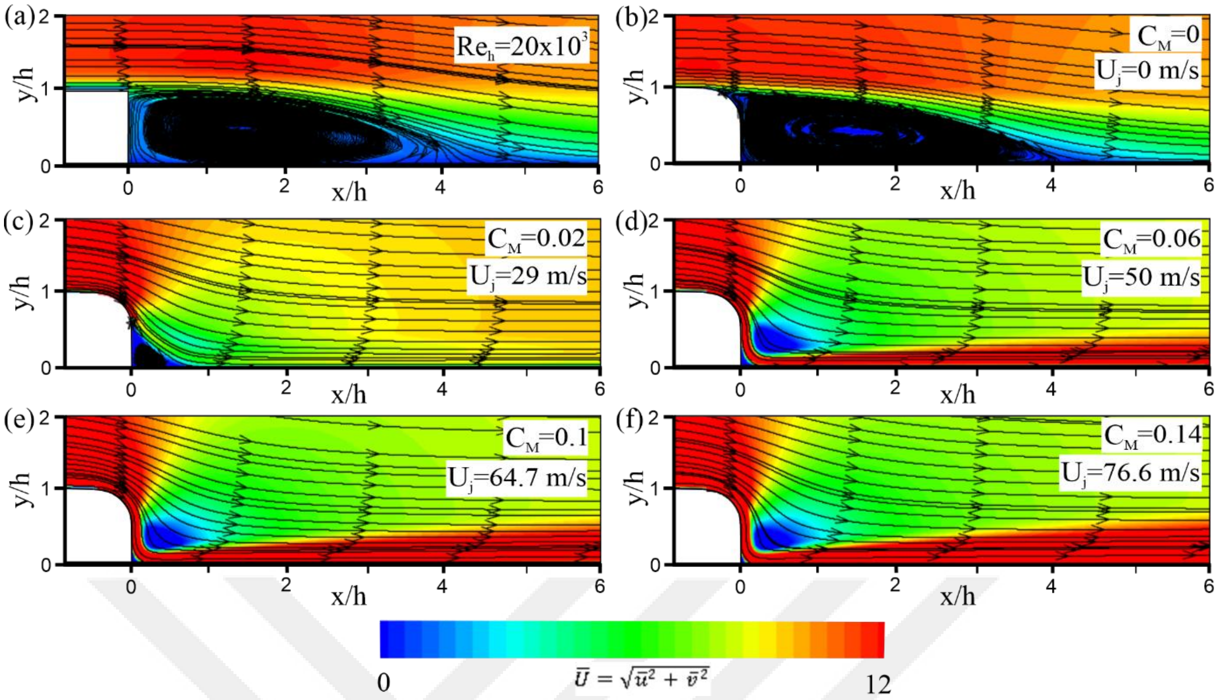

Figure 4.9. Time-averaged streamlines, $\bar{\psi}$, and velocity magnitude, $\bar{U} = \sqrt{\bar{u}^2 + \bar{v}^2}$, contours obtained with and without Coanda blowing for $Re_h = 20 \times 10^3$.

The velocity field results of the highest Reynolds number, $\mathrm{Re}_h = 20 \times 10^3$, employed in the present study are presented in Figure 4.9. The secondary recirculation region observed in the case of the Coanda actuator with no blowing for previous Reynolds numbers, i.e., $\mathrm{Re}_h = 6 \times 10^3$ and 9.6×10^3, disappeared for $\mathrm{Re}_h = 20 \times 10^3$ as shown in Figure 4.9(b). Additionally, the low velocity region that formed over the jet flow when cornering was more pronounced for $\mathrm{Re}_h = 20 \times 10^3$, indicating the adverse effect of over-actuation of the Coanda blowing.

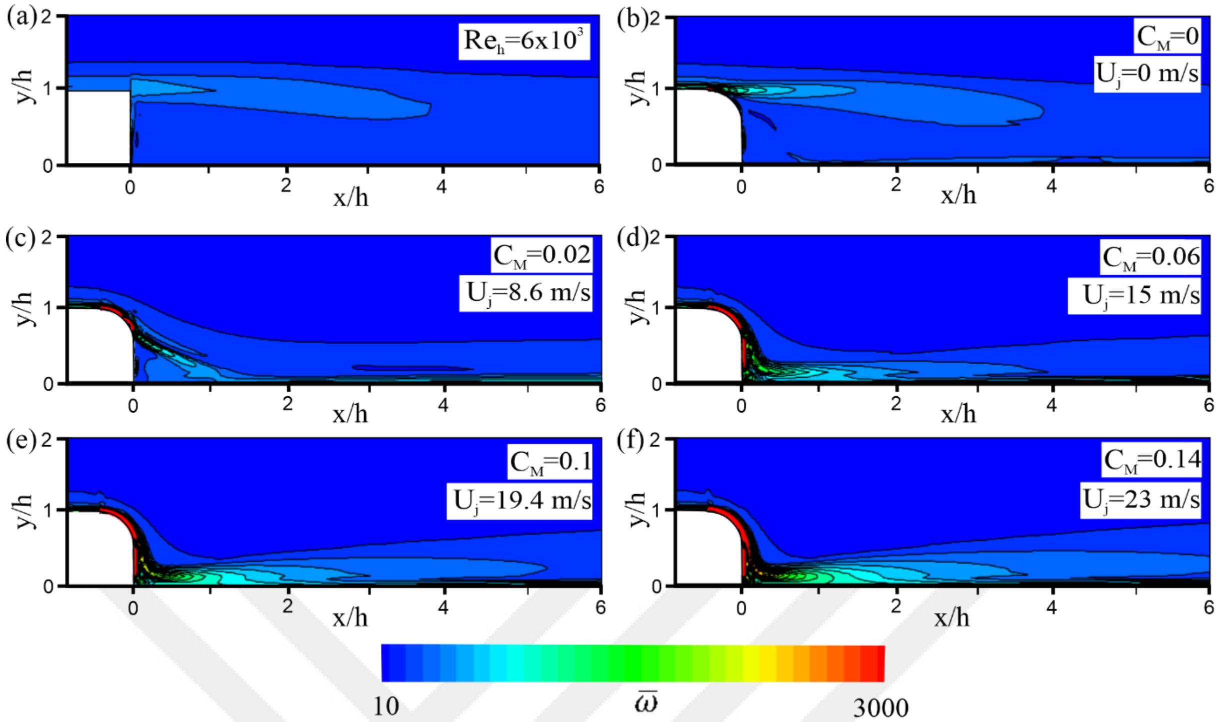

Figure 4.10. Time-averaged vorticity magnitude, $\overline{\omega}$, contours obtained with and without Coanda blowing for $Re_h = 6 \times 10^3$.

The comparison of the time-averaged vorticity, $\overline{\omega}$, concentrations obtained with and without Coanda blowing for the Reynolds numbers of $\mathrm{Re}_h = 6 \times 10^3$, 9.6×10^3 and 20×10^3 are shown in Figure 4.10, 4.11 and 4.12. As presented in Figure 4.10(a-b), after the installation of the Coanda actuator, the vorticity concentrations around the top corner of the BFS increased when compared to the vorticity concentrations occurred in the case with no Coanda actuator. The amount of the vorticity concentrations increased around the top corner of the BFS when the Coanda actuator activated at the momentum coefficient $C_M = 0.02$. Further increasing the momentum coefficient, i.e., $C_M \geq 0.06$, extended the region of high vorticity concentrations downstream while it attached on the Coanda and the BFS surfaces successively, highlighting the effectiveness of Coanda actuator in modifying the flow characteristics.

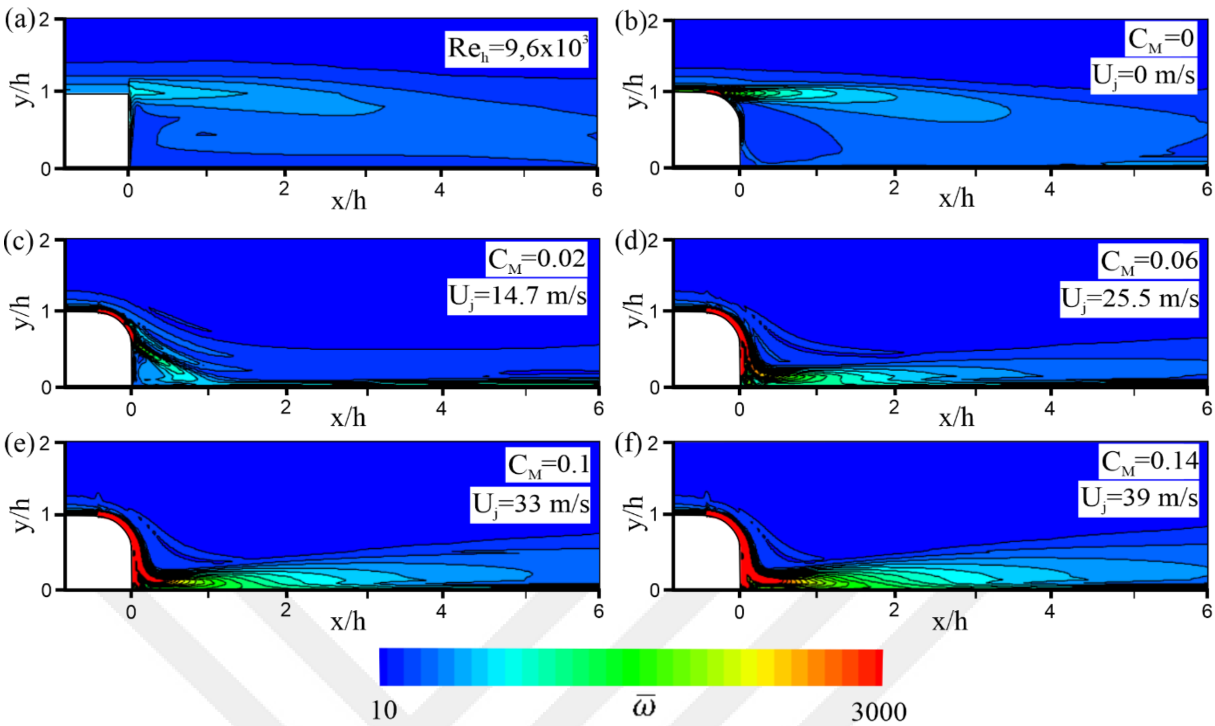

Figure 4.11. Time-averaged vorticity magnitude, $\overline{\omega}$, contours obtained with and without Coanda blowing for $Re_h = 9.6 \times 10^3$.

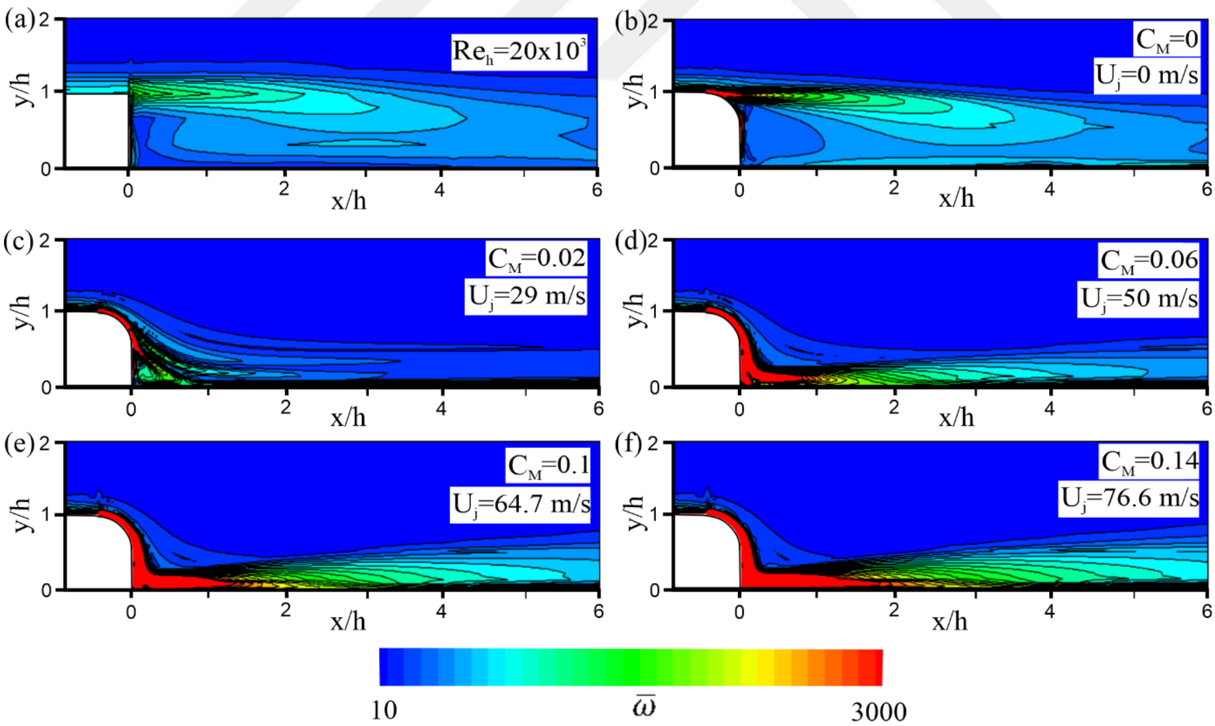

Figure 4.12. Time-averaged vorticity magnitude, $\overline{\omega}$, contours obtained with and without Coanda blowing for $Re_h = 20 \times 10^3$.

The time-averaged vorticity, $\overline{\omega}$, contours given in Figures 4.11 and 4.12 reveal that the amount of the vorticity concentrations and their area covered increase when the Reynolds number of the flow is increased.

4.2.2 Inclined Double Backward Facing Step

This part of the study included the use of passive flow control techniques. For that purpose, inclined-double backward facing step, i.e., DBFS, was used. The reduction of the reattachment length by using single inclined step surfaces in backward-facing step flow was demonstrated in some previous studies (Singh et al. 2011; Choi et al. 2016; Prihoda et al. 2012). However, the use of double-inclined step surfaces for the backward-facing step flow was not implemented previously. The height of the DBFS, i.e., the height of the step surface, was the same as the height of the BFS as given in Figure 3.1 in the previous section. However, the step surface of the BFS was divided into two halves equally so that each inclined surface of the DBFS was obtained. Additionally, each half of the DBSF had different inclination angles with the axial flow direction. For example, the angles of the upper half of the DBFS were α = 15°, 75° and 90° while the angles of the lower half of the DBFS were β = 15°, 30°, 45°, 60°, 75°. Thus, the nine different combinations of the inclined surfaces were used in the investigations as shown in Table 4.1. In the study, α and β are for upper and lower step surface inclination angles, respectively.

Table 4.1. The results of the dimensionless reattachment length, X_r/h obtained for the double backward-facing step with different step surface inclination angles

α (°)	15			90			75		
β (°)	45	60	70	15	30	45	15	30	45
X_r/h(-)	3.32	3.30	3.28	4.80	4.60	4.90	4.8	6.12	6.08

The results of the dimensionless reattachment length, X_r/h for the double backward-facing step with different step surface inclination angles are given in Table 4.1. The reattachment length, X_r/h, was decreased significantly in the combinations of α = 15^o with β = 45^o, 60^o and 70^o.

Nevertheless, it should be noted that the reattachment length, X_r/h, decreased further as the angle of the lower inclined surface, β, was increased. When compared to the reattachment length obtained in the case of unmodified BFS geometry, i.e., X_r/h = 4.16, the maximum relative percent reduction of the reattachment length, X_r/h ,was 20.2%. On the other hand, the other inclined surface combinations, including α = 75° and 90°, resulted longer reattachment length than the one obtained with unmodified BFS geometry.

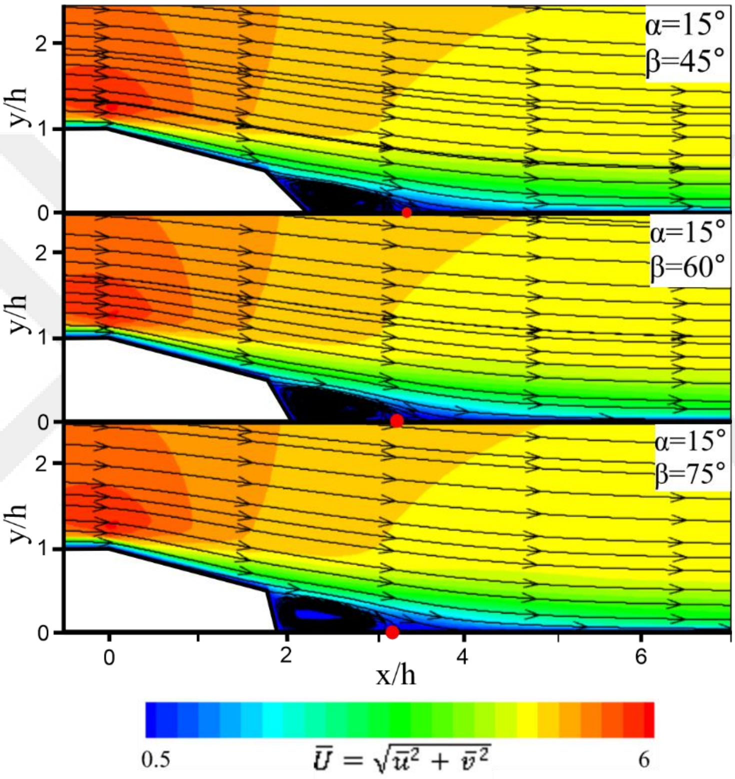

Figure 4.13. The time-averaged streamlines, $\bar{\psi}$, and velocity magnitude, $\overline{U} = \sqrt{\bar{u}^2 + \bar{v}^2}$, contours obtained for different inclined step surface angle combinations, α=15° and β=45°, 60°, 75°.

The time-averaged streamlines, $\bar{\psi}$, and velocity magnitude, $\overline{U} = \sqrt{\bar{u}^2 + \bar{v}^2}$, results obtained for different inclined step surface angle combinations are presented in Figures 4.13, 4.14 and 4.15. As presented in Figure 4.13, the flow did not separate over the upper inclined step surface with α = 15°. However, the flow separated at the trailing edge of the upper inclined step surface whatever the inclination angle of the subsequent lower inclined surface, i.e., β = 45°, 60° and

70°. As a result, the small recirculation region developed downstream of the lower inclined surface. Nevertheless, the reattachment location of the flow on the lower wall of the channel in combinations of inclined step surface angles of α = 15° and β = 45°, 60°, 75° were less than the one obtained with the unmodified BFS geometry.

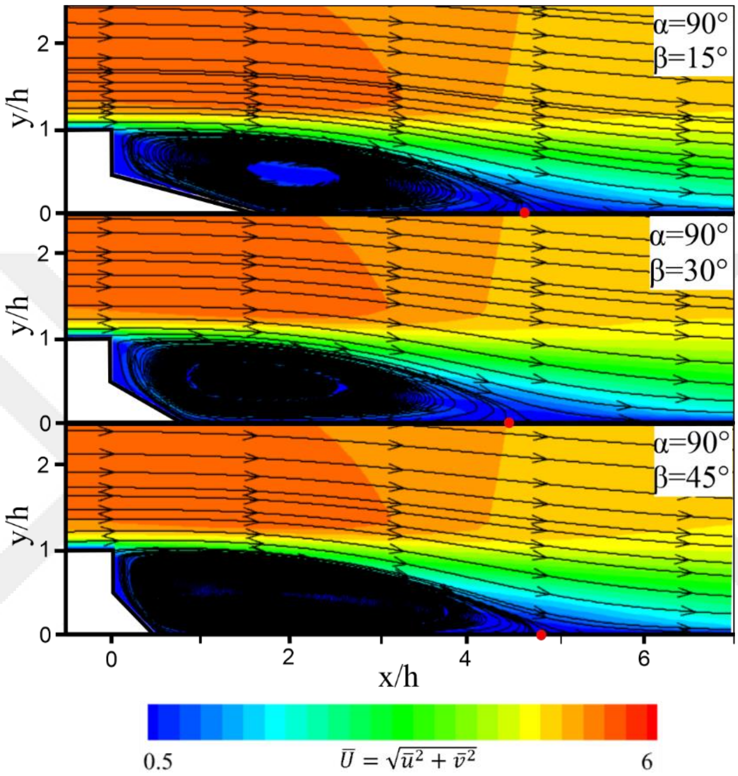

Figure 4.14. The time-averaged streamlines, $\bar{\psi}$, and velocity magnitude, $\bar{U} = \sqrt{\bar{u}^2 + \bar{v}^2}$, contours obtained for the combinations of inclined step surface angles of α=90° and β=15°, 30°, 45°.

Figure 4.14 presents the comparison of the time-averaged streamlines, $\bar{\psi}$, and the velocity magnitude, $\bar{U} = \sqrt{\bar{u}^2 + \bar{v}^2}$, results obtained for the combinations of inclined step surface angles of α=90° and β=15°, 30°, 45°. When compared to the size of the downstream recirculation region obtained in the case of unmodified BFS, the recirculation length results of the combination of the inclined step surfaces given in Figure 4.14 caused the downstream recirculation region to enlarge whatever the inclination angle of the lower step surface, i.e., β=15°, 30°, 45°.

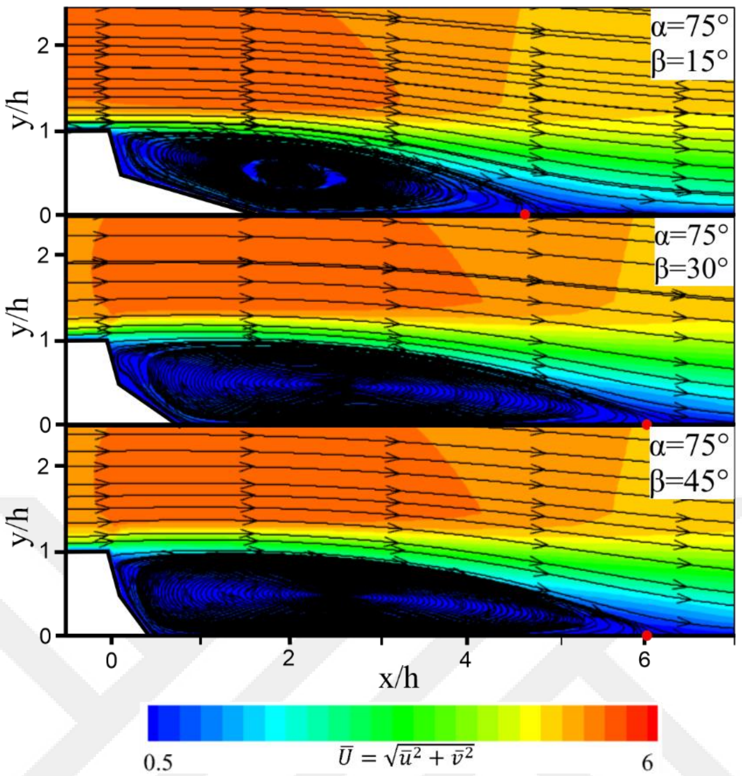

Figure 4.15. Time-averaged streamlines, $\bar{\psi}$, and velocity magnitude, $\overline{U} = \sqrt{\bar{u}^2 + \bar{v}^2}$, contours obtained for the combinations of inclined step surface angles of α=75° and β=15°, 30°, 45°.

A new combinations of inclined step surfaces were obtained by modifying the upper inclined step surface of the inclined step surface combinations given in Figure 4.14 to have an inclination angle of α=75° instead of α=90° with the same lower step surface inclination angles. Thus, the comparisons of time-averaged streamlines, $\bar{\psi}$, and velocity magnitude, $\overline{U} = \sqrt{\bar{u}^2 + \bar{v}^2}$, results of the combinations of inclined step surface angles of α = 75° and β=15°, 30°, 45° are given in Figure 4.15. The results showed that the combination of these inclined step surface angles caused the longest reattachment length in all combinations of the inclined step surface angles considered in this study. Additionally, increasing the inclination angle of the lower step surface, e.g., increasing from β=15° to β=30° or 45°, enlarged the reattachment length.

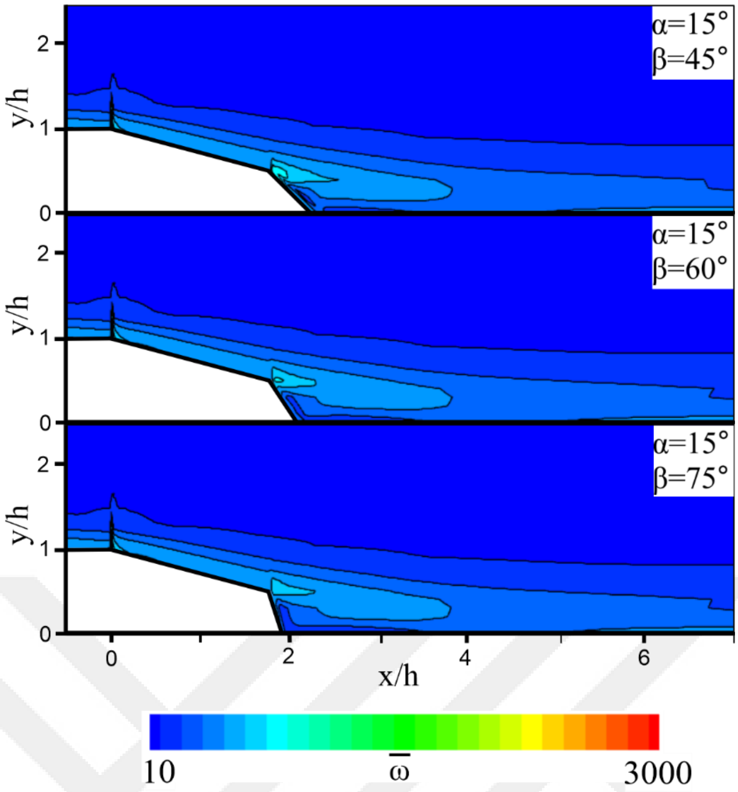

Figure 4.16. The time-averaged vorticity, $\overline{\omega}$, contours obtained for the combinations of inclined step surface angles of α=15° and β=45°, 60°, 75°.

The comparison of the time-averaged vorticity, $\overline{\omega}$, concentrations obtained for various combinations of the inclination angles of the upper and lower step surfaces, α and β, are given in Figures 4.16, 4.17, and 4.18. In Figure 4.16, which shows the configurations of α=15° with varying β values, the vorticities were concentrated at the trailing edge of the upper inclined step surface with α=15°. The amount of the vorticity concentrations decreased slightly as the inclination angle of the lower step surface, β, increased which caused less turbulence in the subsequent shear layer and allowed it to reattach at an earlier point. This result confirmed the slight decrease observed in the reattachment length of inclined step surface angle, α=15° and β=45°, 60°, 75° combinations presented in Table 4.1.

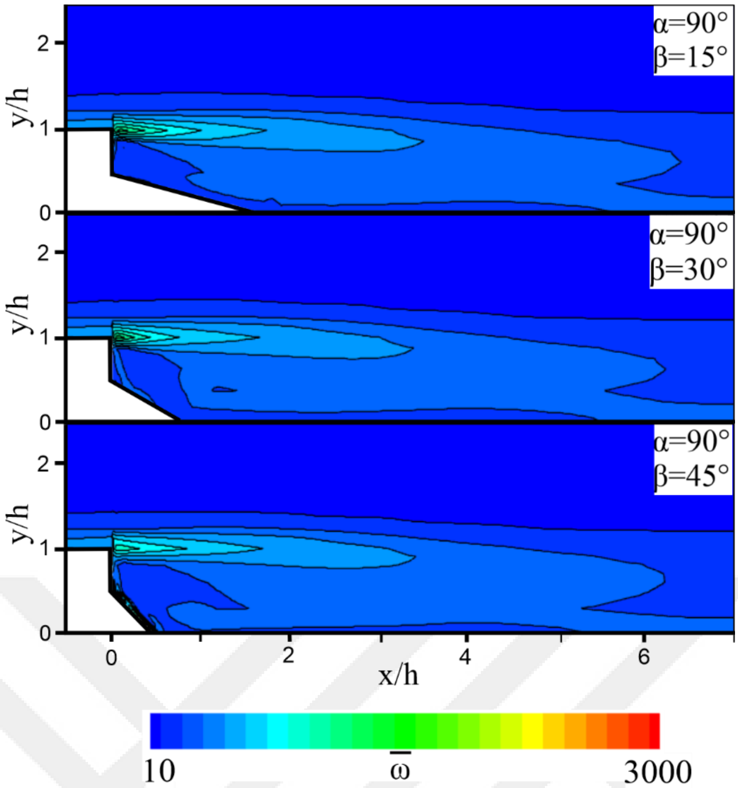

Figure 4.17. The time-averaged vorticity, $\overline{\omega}$, contours obtained for the combinations of inclined step surface angles of α=90° and β=15°, 30°, 45°.

Figure 4.17 compares the vorticity concentration results obtained for the combinations of inclined step surface angles of α=90° and β=15°, 30°, 45°. The contours of the vorticity concentrations together with the shear layer that formed downstream of the upper corner of the step aligned parallel to the axial direction of the freestream flow, indicating the large recirculating regions and reattachment length. Additionally, the comparisons of the vorticity concentrations obtained as the results of the combinations of α=75° and β=15°, 30°, 45°, are given in Figure 4.18.

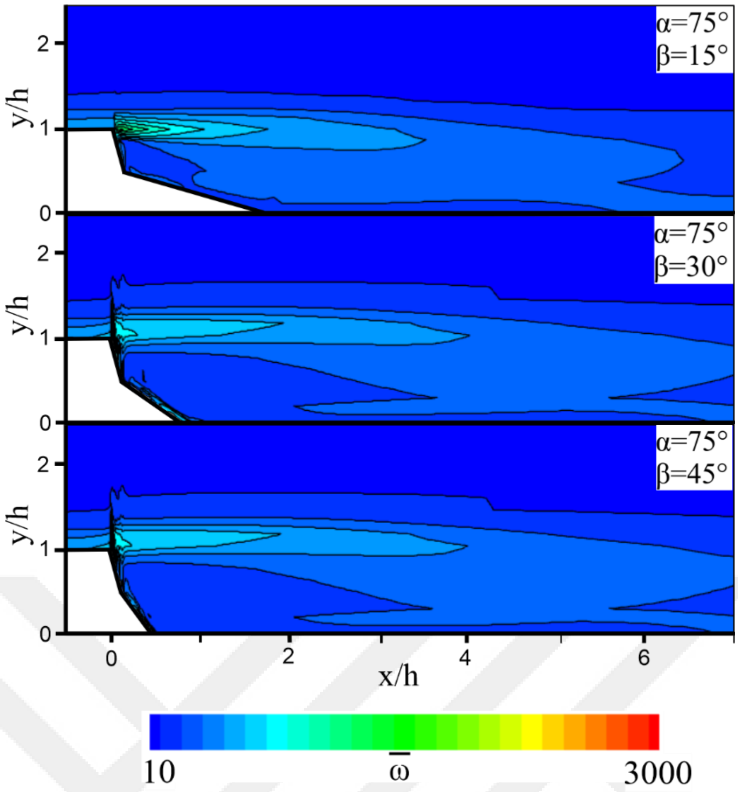

Figure 4.18. The time-averaged vorticity, $\overline{\omega}$, contours obtained for the combinations of inclined step surface angles of α=75° and β=15°, 30°, 45°.

5. CONCLUSION

The present study investigated the characteristics of the flow over the backward-facing step, BFS, with the expansion ratio of H_o/H_i = 1.08 at different Reynolds numbers, i.e., Re_h = 6×10^3, 9.6×10^3, 20×10^3, using numerical methods. Additionally, both active and passive flow control methods were used to control the characteristics of the separated flow downstream of the BFS.

Three different turbulence models, i.e., Spalart-Almaras, realizable k-ε and SST k-ω turbulence models, were tested for the solution of the flow over the backward-facing step. The Spalart-Allmaras turbulence model estimated the reattachment length, X_r, with an error of 0.95%. On the other hand, the SST k-ω turbulence model estimated the axial velocity with a maximum error of 5% in the recirculation region. Additionally, the SST k-ω resolved the secondary recirculation region whereas the Spalart-Allmaras turbulence model failed to resolve this secondary recirculation region.

The blowing using the Coanda actuator at the momentum coefficient of C_M = 0.02, reduced the reattachment length drastically to X_r/h = 1.0, 0.58 and 0.56 for Re_h = 6×10^3, 9.6×10^3, 20×10^3, respectively. Using a larger momentum coefficient, i.e., $C_M \geq 0.06$, completely vanished the recirculation region, indicating that the use of a higher momentum coefficient than C_M = 0.02 was not meaningful.

In the case of passive flow control via inclined double backward-facing step, the maximum relative percent reduction of the reattachment length was 20.2% using the combinations of the inclination angle of upper step surface, α = 15°, and lower step surface, β = 70°. On the other hand, the other inclined surface combinations, including α = 75° and 90°, resulted longer reattachment length than the one obtained with unmodified BFS geometry.

Overall, the Coanda actuator effectively reduced the reattachment length and altered flow characteristics, with the optimal results at C_M=0.02. On the other hand, using an inclined surface on the upper part of the step of the BFS had a significant impact on the reattachment length.

REFERENCES

Abu-Nada E. (2008). Application of nanofluids for heat transfer enhancement of separated flows encountered in a backward-facing step. International Journal of Heat and Fluid Flow 29 242–249.Z

Addad Y., Laurence D., Talotte C., and Jacob M.C., (2003). Large eddy simulation of a forward–backward-facing step for acoustic source identification. *International Journal of Heat and Fluid Flow 24 562–571.*

Al-Jelawy H., Kaczmarczyk S., AlKhafaji D., Mirhadizadeh S., Lewis R., Cross M. (2016). A Computational Investigation of a Turbulent Flow Over a Backward Facing Step with OpenFOAM. *9th International Conference on DevelopmFents in eSystems Engineering.*

Armaly B.F., Durst F., Jose c f Pereira (1983). Experimental and Theoretical Investigation of Backward-Facing Step Flow. *Journal of Fluid Mechanics, 127:473 – 496*

Avancha R.V.R., and Pletcher R.H. (2002). Large eddy simulation of the turbulent flow past a backward-facing step with heat transfer and property variations. *International Journal of Heat and Fluid Flow 23 601–614.*

Barri M. and Andersson H. (2010). Turbulent flow over a backward-facing step. Part 1. Effects of anti-cyclonic system rotation. *J. Fluid Mech., vol. 665, pp. 382–417.*

Barros D., Borée J., Noack B. R., Spohn A. and Ruiz R. (2016). Bluff body drag manipulation using pulsed jets and the Coanda effect. *J. Fluid Mech., vol. 805, pp. 422_459*

Benard N., Patricia S., Bonnet J., et al. (2016) Control of the coherent structure dynamics downstream of a backward-facing step by DBD plasma actuator. *International Journal of Heat and Fluid Flow 61 158–173.*

Benavides A. and vanWachem B. (2009) Eulerian-Eulerian prediction of dilute turbulent gas-particle flow in a backward-facing step. *International Journal of Heat and Fluid Flow Volume 30, Issue 3*

Bredberg J. and Davidson L. (2004) Low-Reynolds Number Turbulence Models: An Approach for Reducing Mesh Sensitivity. *J. Fluids Eng. Jan 2004, 126(1): 14-21*

Bouda N. N., Schiestel R., Amielh M., Rey C., and Benabid T. (2008) Experimental approach and numerical prediction of a turbulent wall jet over a backward-facing step. *International Journal of Heat and Fluid Flow 29 927–944.*

Chen L., Asai K., Nonomura T., Xi G., Liu T. (2018). A review of Backward-Facing Step (BFS) flow mechanisms, heat transfer and control. *Thermal Science and Engineering Progress, Volume 6, June 2018, Pages 194-216*

Choi H. H., Nguyen V. T., and Nguyen J. (2016) Numerical Investigation of Backward Facing Step Flow Over Various Step Angles. *Procedia Engineering 154 420 – 425.*

Choi S.W., and Kim H. S. (2020). Predicting turbulent flows in butterfly valves with the nonlinear eddy viscosity and explicit algebraic Reynolds stress models. *Phys. Fluids 32, 085105*

Chovet C., Lippert M., Keirsbulck L., Foucaut J. (2018) Unsteady Behaviour of a Backward-facing Step in Forced Flow. *Flow Turbulence Combust* **102**, 145–165 (2019).

Chun K. B. and Sung H. J. (1996). Control of turbulent separated flow over a backward-facing step by local forcing. *Experiments in Fluids 21 0996) 417-426*

Cramer K.R., (1958). On laminar separation babble, *J. Aeronaut. Sci. 25 143–144*

D'Adamo J., Sosa R. and Artana G. (2014). Active control of a backward-facing step flow with plasma actuators. *Journal of Fluids Engineering, Dec 2014, 136(12): 121105 (9 pages).*

Dejoan A., and Leschziner M.A. (2004) Large eddy simulation of periodically perturbed separated flow over a backward-facing step. *International Journal of Heat and Fluid Flow 25 581–592.*

Deng, F., Han, G., Liu, M., Ding, J., 2019. Numerical simulation of the interaction of two shear layers in double backward-facing steps. *Phys. Fluids, 31, 056106; doi: 10.1063/1.5083986.*

Durst F. and Tropeac. (1981). Flows over Two-Dimensional Backward — Facing Steps. *In: Dumas, R., Fulachier, L. (eds) Structure of Complex Turbulent Shear Flow. International Union of Theoretical and Applied Mechanics. Springer, Berlin, Heidelberg.*

Durst F. and Tropeac. (1981) Turbulent, backward-facing step in two-dimensional ducts and channels. In: *Proc. Turbulent Shear Flow* 3 *Symp. Datvk.*

Durst F. (2008) An Introduction to the Theory of Fluid Flows. Springer-Verlag Berlin Heidelberg

Englar R.J. (1971). Two-dimensional transonic wind tunnel tests of three 15-percent thick circulation control airfoils.

Fessler J.R., and, Eaton J.K. (1999) Turbulence modification by particles in a backward-facing step flow. *J. Fluid Mech. (1999), vol. 394, pp. 97-117*

Furuichi N., Hachiga T., and Kumada M., (2004) An experimental investigation of a large-scale structure of a two-dimensional backward-facing step by using advanced multi-point LDV. *Experiments in Fluids 36(2):274-281*

Geropp D. and Odenthal H. J., (2000). Drag reduction of motor vehicles by active flow control using the Coanda effect. *Experiments in Fluids volume 28, pages74–85*

Guo Z.Y., Li D.Y., Liang X.G., (1996). Thermal effect on the recirculation zone in sudden expansion gas flows, *Int. J. Heat Mass Transfer 39 2619–2624*.

Hammad, K.J., 2015. The Flow Behavior of a Biofluid in a Separated and Reattached Flow Region. *Journal of Fluids Engineering, Vol. 137, 061104-1.*

Hasan, M. a. Z., 1992. The flow over a backward-facing step under controlled perturbation: laminar separation. *Journal of Fluid Mechanics 238, 73–96*.

Hasan, M.A.Z., Khan, A.S., 1992. On the instability characteristics of a reattaching shear layer with nonlaminar separation. *International Journal of Heat and Fluid Flow 13, 224–231*.

Hu R., Wang L., and Fu S. (2020). Modelling and Numerical Simulation for Flow Control. Advances in Effective Flow Separation Control for Aircraft Drag Reduction. *Computational Methods in Applied Sciences, vol 52. Springer, Cham.* https://doi.org/10.1007/978-3-030-29688-9_16

Huang, H.T., Fiedler, H.E., 1997. A DPIV study of a starting flow downstream of a backward-facing step. *Experiments in Fluids 23, 395–404.*

Jahanmiri M. (2010). Active Flow Control: A Review. *Chalmers University of Technology, Research report 2010:12.*

Jones G. S., Viken S. A., Washburn A. E., Jenkins L. N., Cagle C. M. (2002) An Active Flow Circulation Controlled Flap Concept for General Aviation Aircraft Applications. *1st Flow Control Conference AIAA 2002-3157*

Jovic and Driver (1994) Backward-facing step measurements at low Reynolds number. *NASA Technical Memorandum 108807*

Juste G. L., Fajardo P., and Guijarro A. (2016). Assessment of secondary bubble formation on a backward-facing step geometry. *Phys. Fluids 28, 074106.*

Kang S., and Choi H., (2002) Suboptimal feedback control of turbulent flow over a backward-facing step. *J. Fluid Mech. (2002), vol. 463, pp. 201-227.*

Kapiris P.G., and Mathioulakis D.S., (2014) Experimental study of vortical structures in a periodically perturbed flow over a backward-facing step. *International Journal of Heat and Fluid Flow 47 101–112*

Kasagi N. and Matsunaga A. (1995). Three-dimensional particle-tracking velocimetry measurement of turbulence statistics and energy budget in a backward-facing step flow. *International Journal of Heat and Fluid Flow Volume 16 477-485.*

Khuwaranyu K. and Putivisutisak S. (2009). Combined low-Reynolds-number k–w model with length scale correction term for recirculating flows. *Journal of Engineering and Technology Research Vol.1 (8), pp.171-180*

Kim J., Kline S.J., Johnston J. P. (1980) Investigation of a Reattaching Turbulent Shear Layer: Flow Over a Backward-Facing Step. *J. Fluids Eng., 102(3): 302-308*

Ko, S., 1999. A near-wall Reynolds stress model for backward-facing step flows. *KSME International Journal 13, 200–210.* https://doi.org/10.1007/BF02943672

Kostas J., Soria J. and Chong M.S. Particle image velocimetry measurements of a backward-facing step flow. *Experiments in Fluids 33 838–853*

Kumar A.S., Singh A., and Thiagarajan K. B. (2020) Simulation of backward facing step flow using OpenFOAM. *AIP Conference Proceedings 2204, 030002*

Lee T. and Mateescu D. (1998). Experimental and Numerical Investigation of of 2-D Backward-facing Step Flow. *Journal of Fluids and Structures, Volume 12, Issue 6, August 1998, Pages 703-716*

Le H., Moin P. and Kim J. (1997) Direct numerical simulation of turbulent flow over a backward-facing step. *Journal of Fluid Mechanics / Volume 330 pp 349 374*

Li, Z., Di Zhang, Liu Y., Wu C., and Gao N. (2020) Effect of periodic perturbations on the turbulence statistics in a backward-facing step flow. *Physics of Fluids 32,*

Louda P., Príhoda J, Kozel K., Svácek P. (2013). Numerical simulation of flows over 2D and 3D backward-facing inclined steps. *International Journal of Heat and Fluid Flow 43 268–276.*

Lubert, C. (2011) On Some Recent Applications of the Coanda Effect. *International Journal of Acoustics and Vibration, Vol. 16, No. 3,*

Manosalvas D. E., Economon T. D., Palacios F. and Jameson A. (2015) Techniques for the Design of Active Flow Control Systems in Heavy Vehicles. *AIAA -3312*

Manosalvas D. E., Economon T. D., Othmer C. and Jameson A. (2016) Computational Design of Drag Diminishing Active Flow Control Systems for Heavy Vehicles. *AIAA-4082*

Ma X., Geisler R. & Schröder A. (2017) Experimental Investigation of Separated Shear Flow under Subharmonic Perturbations over a Backward-Facing Step. *Flow Turbulence Combust* 99, 71–91.

Ma X., Geisler R. and Schröder A. (2017) Experimental Investigation of Three-Dimensional Vortex Structures Downstream of Vortex Generators Over a Backward-Facing Step. Flow, *Turbulence and Combustion volume 98, pages389–415*

Mehrez Z., Bouterra M., El Cafsi A., Belghith A. and Le Quéré P., (2010) Active control of flow behind a backward facing step by using a periodic perturbation. *ARPN Journal of Engineering and Applied Sciences Vol. 5, No. 2*

Menter F. R. (1994) Two-equation eddy-viscosity turbulence models for engineering applications. *AIA A Journal Vol. 32, No. 8.*

Mohammad A. Hossain M.A., Rahman Md. T. and Ridwan S. (2013) Numerical Investigation of Fluid Flow Through A 2D Backward Facing Step Channel. *International Journal of Engineering Research & Technology Vol. 2 Issue 10*

Moore T.W.F., (1960). Some experiments on the reattachment of a laminar boundary layer separating from a rearward-facing step on a flat plate aerofoil, *J. R. Aero. Soc. 64 668–672.*

Munters W., Koloszar L. and Planquart P. (2022) Numerical simulation of a confined backward-facing step flow using hybrid turbulence models in OpenFOAM. *The 18th International Conference on Fluid Flow Technologies*

Mushyam A. and Bergada J. M. (2015) Active Flow Control on Laminar flow over a Backward facing step. *J. Phys.: Conf. Ser. 633 012110.*

Mushyam, A., Bergada, J.M., Navid Nayeri, C., (2016). A numerical investigation of laminar flow over a backward facing inclined step. *Meccanica 51, 1739–1762.*

Nakagawa H. and Nezu I. (2010) Experimental investigation on turbulent structure of backwardfacing step flow in an open channel. *Journal of Hydraulic Research, 25:1, 67-88*

Okada K., Nonomura T., Fujii K. and Miyaji K. (2012). Computational Analysis of Vortex Structures Induced by a Synthetic Jet to Control Separated Flows. *International Journal of Flow Control, Volume 4 · Number 1+2*

O'Malley K., Fitt A.D., Jones T.V., Ockendon J.R., Wilmott P. (1991) Models for highReynolds-number flow down a step, *J. Fluid Mech. 222 139–155.*

Ötügen M.V. (1991). Expansion ratio effects on the separated shear layer and reattachment downstream of a backward-facing step. *Experiments in Fluids 10, 273-280.*

Pain, R., Weiss, P.-E., Deck, S., Robinet, J.-C., 2019. Large scale dynamics of a high Reynolds number axisymmetric separating/reattaching flow. *Physics of Fluids 31, 125119.* https://doi.org/10.1063/1.5121587

Papadopoulos G. and Ötügen M.V. (1995). Separating and Reattaching Flow Structure in a Suddenly Expanding Rectangular Duct. *J. Fluids Eng., 117(1): 17-23.*

Pfeiffer J. and King R., (2012) Multivariable Closed-Loop Flow Control of Drag And Yaw Moment For A 3D Bluff Body. *6th AIAA Flow Control Conference 25 – 28*

Pont-Vilchez A., Trias F. X., Gorobets A. and Oliva A. (2019). Direct numerical simulation of backward-facing step flow at $Re_\tau = 395$ and expansion ratio 2. *J. Fluid Mech. (2019), vol. 863, pp. 341–363.*

Prihoda J., Kotek M., Uruba V., Kopecky V., Hladik O. (2012) Experimental investigation of turbulent flow in a channel with the backward-facing inclined step. *EPJ Web of Conferences 25, 01080.*

Rani H.P., Sheu T.W.H., and Tsai E.S.F. (2007) Eddy structures in a transitional backward-facing step flow. *J. Fluid Mech., vol. 588, pp. 43–58.*

Rhee G.H., and Sung H. J., (1999) Numerical prediction of locally forced turbulent separated and reattaching flow. *Fluid Dynamics Research 26 421-436*

Schram, C., Rambaud, P. & Riethmuller, M.L. (2004) Wavelet based eddy structure eduction from a backward facing step flow investigated using particle image velocimetry. *Exp Fluids* 36, 233–245

Singh A. P., Paul A. R., and Ranjan P. (2011) Investigation of reattachment length for a turbulent flow over a backward facing step for different step angle. *International Journal of Engineering, Science and Technology Vol. 3, No. 2, pp. 84-88.*

Spazzini P. G., Iuso G., Onorato M., et al. (2001) Unsteady Behaviour of Back-facing Step Flow. *Experiments in Fluids* **30**, 551–561

Sujar-Garrido P., Benard N. Moreau E. and Bonnet J. P. (2015) Dielectric barrier discharge plasma actuator to control turbulent flow downstream of a backward-facing step. *Experiments in Fluids volume 56, Article number: 70*

Tihon J., Legrand J. and Legentilhomme P. (2001). Near-Wall Investigation of Backward-facing Step Flows. *Experiments in Fluids volume 31, pages484–493*

Uruba V., Jonas P. and Mazur O. (2007). Control of a channel-flow behind a backward-facing step by suction/blowing. *International Journal of Heat and Fluid Flow 28 665-672.*

Velikorodyny A., Duck G., and Oshkai P. (2010) Experimental investigation of flow over a backward-facing step in proximity to a flexible wall. *Experiments in Fluids volume 49, pages167–181 (2010).*

Yanhua Wu, Huiying Ren and Hui Tang (2013). Turbulent flow over a rough backward-facing step. *International Journal of Heat and Fluid Flow 44 (2013) 155–169.*

Yoshioka S., Obi S., & Masuda S. (2001). Turbulence statistics of periodically perturbed separated flow over backward-facing step. *International Journal of Heat and Fluid Flow 22 393-401.*

Yu K., Hao J., Wen C. Y., and Xu J. (2024). Bi-global stability of supersonic backward-facing step flow. *J. Fluid Mech. (2024), vol. 981, A29.*

Zouhaier M., Mourad B., Afif El Cafsi, Ali B. and Patrick Le Quéré (2010). Active control of flow behind a backward facing step by using a periodic perturbation. *ARPN Journal of Engineering and Applied Sciences VOL. 5, NO. 2.*

Wang F., Gao A., Wu S., Zhu S., Dai J. and Liao Q. (2019). Experimental Investigation of Coherent Vortex Structures in a Backward-Facing Step Flow. *Water; 11(12):2629.*

Wilcox, David C. (2006). Turbulence Modelling for CFD. DCW Industries, Inc, 5354 Palm Drive, La Cafiada, California

Wu Y., Ren H., and Tang H. (2013). Turbulent flow over a rough backward-facing step. *International Journal of Heat and Fluid Flow 44 155–169.*

APPENDİX

Appendix A

Englar (1971) generated a hypothesis to understand the most effective Coanda control geometry for the airfoil studies as seen in Figure A.1. Chord ratio (c) and Coanda radius (r) are the two parameters to choose the slot height (s). The chord ratio is the size of the wing in the streamwise direction in the literature. The chord length was assumed to be the length of the lower entrance wall, L_{ent} in this study. The most effective region is shown in Figure 3.2. According to Figure 3.2, parameters were assumed that s/c=0.0015 and s/r=0.04 to choose the most efficient slot geometry.

$$\frac{s}{c} = 0.0015 \quad \text{(A.1)}$$

$$c = L_{ent} = 0.3 \text{ m} \quad \text{(A.2)}$$

so;

$$s = 0.45 \text{ mm} \quad \text{(A.3)}$$

then;

$$\frac{s}{r} = 0.04 \quad \text{(A.4)}$$

$$r = 11.25\text{mm} \quad \text{(A.5)}$$

Momentum coefficient, C_M is given as follows (Englar, 1971).

$$C_M = \frac{\dot{m}U_j}{\frac{1}{2}\rho U_\infty^2 A_h} \quad \text{(A.6)}$$

Where, U_j is the Coanda velocity, $\dot{m}$ is the mass flow rate, A_s is the Coanda cross-sectional area and A_h is the step cross-sectional area. The equation of mass flow rate, $\dot{m}$, is given as follows.

$$\dot{m} = \rho U_j A_s \quad \text{(A.7)}$$

The velocity magnitude at the second inlet is represented by U_j and it was determined by equation (A.6) assuming a range of C_M is 2×10^{-2} to 1.4×10^{-1}. In the previous studies, the most efficient determined as 2×10^{-2} as seen in the study of Preiffer and King (2014) and Haffner et al. (2020). So, C_M assumed as minimum $C_M = 2 \times 10^{-2}$ and four different C_M were used in this study.

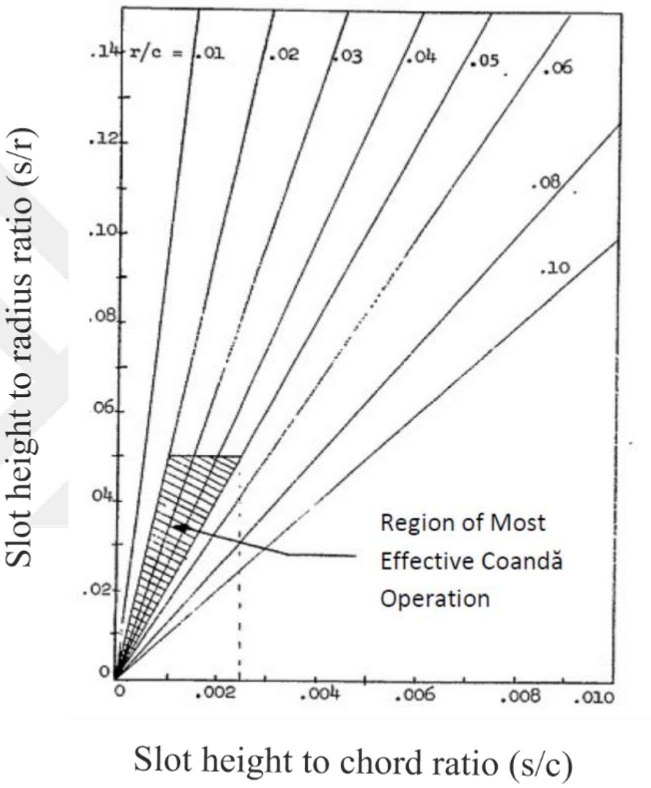

Figure A.1. The most effective Coanda control geometry